Mechanics Based Design of Structures and Machines
An International Journal

ISSN: (Print) (Online) Journal homepage: https://www.tandfonline.com/loi/lmbd20

The optimum inerter-based additional viscoelastic mass dampers for dynamic response mitigation of structures

Sudip Chowdhury, Arnab Banerjee & Sondipon Adhikari

To cite this article: Sudip Chowdhury, Arnab Banerjee & Sondipon Adhikari (10 May 2023): The optimum inerter-based additional viscoelastic mass dampers for dynamic response mitigation of structures, Mechanics Based Design of Structures and Machines, DOI: 10.1080/15397734.2023.2209460

To link to this article: https://doi.org/10.1080/15397734.2023.2209460

MECHANICS BASED DESIGN OF STRUCTURES AND MACHINES
https://doi.org/10.1080/15397734.2023.2209460

The optimum inerter-based additional viscoelastic mass dampers for dynamic response mitigation of structures

Sudip Chowdhury[a], Arnab Banerjee[a], and Sondipon Adhikari[b]

[a]Civil Engineering Department, Indian Institute of Technology Delhi, India; [b]James Watt School of Engineering, The University of Glasgow, Glasgow, Scotland, UK

ABSTRACT

The additional inerter-based viscoelastic mass dampers (AIVMD) and additional viscoelastic mass damper inerters (AVMDI) are introduced in this article. H_2 and H_∞ optimization schemes are utilized to derive the optimal closed-form solutions for these novel dampers analytically. A parametric study performs to investigate the sensitivity of the optimal design parameters with other system parameters such as damper mass ratio, inerter mass ratio, and stiffness ratio. Thus, a higher damper mass ratio, a higher inerter mass ratio, and a higher stiffness ratio are recommended to design optimum novel dampers for achieving robust vibration reduction capacities. Therefore, H_2 optimized AIVMD and AVMDI have 53.23% and 57.73% dynamic response reduction capacities while H_∞ optimized AIVMD and AVMDI can provide 72.97% and 75.57% dynamic response reduction capacities subjected to harmonic excitation, respectively. In addition, random-white noise excitations are also applied instead of harmonic excitation to cross-check the accuracy of the optimal design parameters. The overall result shows that 74.24% and 82.17% dynamic response reduction capacities for H_2 optimized AIVMD and AVMDI, furthermore, 92.14% and 94.36% dynamic response reduction capacities for H_∞ optimized AIVMD and AVMDI. These optimal closed-form solutions are mathematically accurate and relevant for practical applications.

ARTICLE HISTORY
Received 12 December 2022
Accepted 8 February 2023

KEYWORDS
Additional inerter-based viscoelastic mass dampers (AIVMD); additional viscoelastic mass damper inerters (AVMDI); standard linear solid models (SLS); H_2 and H_∞ optimization; dynamic response reduction capacities

1. Introduction

Mass dampers such as tuned mass dampers (Kaynia, Veneziano, and Biggs 1981), tuned inerter dampers (Deastra et al. 2020), and tuned mass damper inerter (Marian and Giaralis 2014) are effective passive vibration control devices to mitigate the dynamic responses of the structures from multi-hazard scenarios (Zuo, Bi, and Hao 2017; Qiao et al. 2022; Petrini, Giaralis, and Wang 2020), earthquakes (De Domenico and Ricciardi 2018; Shen et al. 2019; Djerouni et al. 2021), cyclones (Elias and Matsagar 2018; Wang et al. 2019; Giaralis and Petrini 2017), and high-level water pressure (Zhang and Fitzgerald 2020; Jahangiri, Sun, and Kong 2021; Zhang and Høeg 2021). The energy dissipation through these devices occurs when their natural frequency intersects exactly with the excitation frequency, and out-of-phase conditions happen at this resonating frequency (Marano, Greco, and Sgobba 2010; Pellizzari et al. 2022). Frahm introduces tuned mass damper for undamped dynamic systems without providing optimal design parameters (Frahm 1909). After that, several studies have been conducted on these devices, and different optimization

CONTACT Sudip Chowdhury sudip.chowdhury@civil.iitd.ac.in Civil Engineering Department, Indian Institute of Technology Delhi, India.
Communicated by Francesco Tornabene.

schemes have been applied to determine the optimal design parameters for these mass dampers (Leung et al. 2008; Morga and Marano 2014; Rathi and Chakraborty 2017; Ruiz et al. 2018; Kaveh et al. 2020; Chowdhury and Banerjee 2022b). However, to mathematically derive exact closed-form expressions for these dampers, H_2 and H_∞ optimization schemes are the most prominent and oldest (Chowdhury, Banerjee, and Adhikari 2022b). Den Hartog and Ormondroyd first introduced the H_∞ optimization method for harmonically excited structures as a name of the fixed-point theory, considering damped structures and also providing closed-form expressions for optimal design parameters (Den Hartog 1985). In contrast, the H_2 optimization method applies to the random vibration excited structures (Chowdhury and Banerjee 2022a). Applying both optimization schemes, the mathematical formulations for optimal design parameters are derived analytically (Zhao et al. 2020, 2019).

The inerters are one of the effective mass amplification devices installed inside the tuned mass dampers to increase their vibration reduction capacity without increasing the static mass of the dampers (Smith 2002; Papageorgiou, Houghton, and Smith 2009; Chen and Hu 2019; Wagg 2021). These inerters are placed inside the tuned mass dampers with different structural configurations and produce tuned inerter damper, tuned mass damper inerter, tuned inerter viscous damper, etc. (Ma, Bi, and Hao 2021; Kuhnert et al. 2021; Liu et al. 2022; Zheng, Li, and Zhang 2022). Inertial amplifiers (Chowdhury, Banerjee, and Adhikari 2023) are also one of the effective mass amplification devices (Chowdhury, Banerjee, and Adhikari 2021). However, the effective mass amplifications through inertial amplifiers (Chowdhury, Banerjee, and Adhikari 2022a, 2023) occur through their geometrical configurations, generating the inertial forces, whereas inerter produces effective masses through motion amplifiers. However, all these devices are generally contained viscous damping (Adhikari and Woodhouse 2001a). Non-viscous damping (Adhikari and Woodhouse 2001b) and viscoelastic materials (Adhikari and Pascual 2009) can also be applied to these devices. Only tuned viscoelastic damper (Batou and Adhikari 2019) exists with optimal closed-form solutions using fixed-point theory. Therefore, H_2 optimization method can be applied for the optimization process and also, non-viscous damping and viscoelastic materials can be applied to the inerter-base mass dampers. Thus, a research scope detects and addresses this research gap, and viscoelastic materials are installed inside the inerter-based mass dampers, producing two novel mass dampers, namely, additional inerter-based viscoelastic mass dampers (AIVMD) and additional viscoelastic mass damper inerters (AVMDI).

The mathematical formulations for the optimal design parameters of these novel dampers derive through H_2 and H_∞ optimization schemes. These dampers are installed at the top of single-degree-of-freedom systems, and the vibration reduction capacities of these novel dampers are determined for harmonic and random-white noise.

2. Structural model and equations of motion

The structural diagram of a single degree of freedom system controlled by additional inerter-based viscoelastic mass dampers displays in Fig. 1(a). Besides, another single degree of freedom system controlled by additional viscoelastic mass damper inerters has also been shown in Fig. 1(b). For both controlled structures, m_d and k_d define the mass and the stiffness of the proposed dampers. k_v and c_d are the stiffness and damping of the viscoelastic material induced inside the mass dampers. m_b defines the mass of the inerters. m_s, c_s, and k_s refer to the mass, damping, and stiffness of the single degree of freedom systems (SDOF). u_d and u_s define the unknown degree of freedom of the dampers and the SDOF system. $\ddot{x}_g$ refers to the base excitation.

2.1. Additional inerter-based viscoelastic mass dampers

An additional inerter-based viscoelastic mass dampers (AIVMD) with viscoelastic damping has been shown in Fig. 1(a). The standard linear solid (SLS) models are applied mathematically to

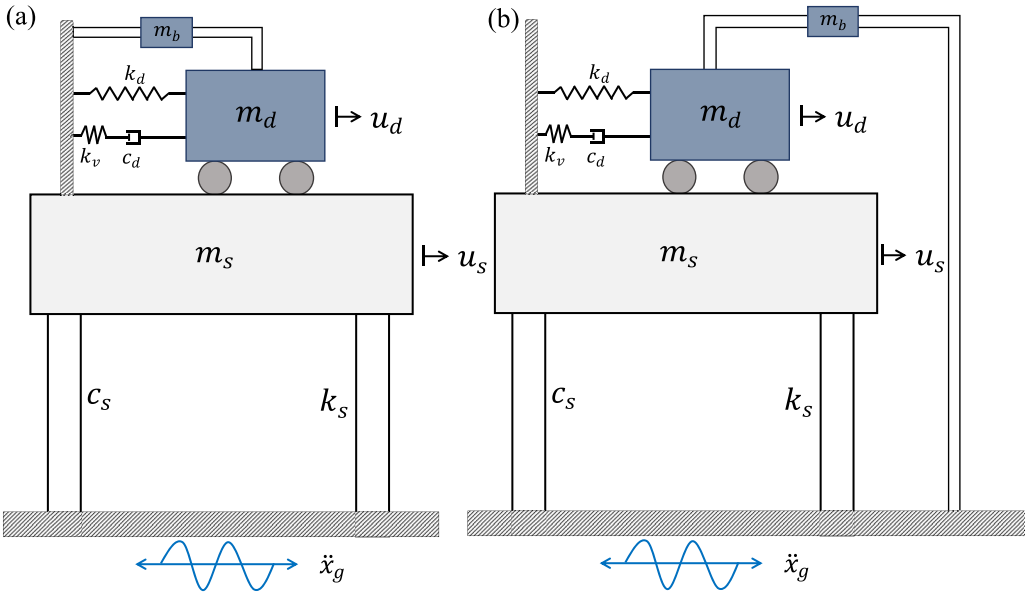

Figure 1. The schematic diagrams of the single degree of freedom systems equipped with (a) additional inerter-based viscoelastic mass dampers and (b) additional viscoelastic mass damper inerters.

formulate the viscoelastic material. Therefore, the governing equation of motion for the additional inerter-based viscoelastic mass damper has been derived as

$$(m_d + m_b)\ddot{x}_d + \Xi\dot{x}_d + k_d x_d = -m_d\ddot{x}_g \tag{1}$$

where $x_d = u_d - u_s$ refers to the relative displacement of AIVMD w.r.t primary structure. Ξ refers to the hereditary function. $\Xi\dot{x}_d$ has been solved by the convolution integral and expressed as

$$\Xi\dot{x}_d = \int_{-\infty}^{t} \Xi(t-\tau)\dot{x}_d(\tau)d\tau \tag{2}$$

The novel tuned mass damper is in the static state at $t = 0$. Therefore, Eq. (1) has been derived as

$$(m_d + m_b)\ddot{x}_d + \int_{-\infty}^{t} \Xi(t-\tau)\dot{x}_d(\tau)d\tau + k_d x_d = -m_d\ddot{x}_g \tag{3}$$

The hereditary function Ξ expresses as $\Xi(t) = k_v e^{-\frac{k_v t}{c_d}}$ and the integrating form is a dirac function at $k_v \to \infty$. The steady state solutions are considered as $x_d = X_d e^{i\omega t}$ and $\ddot{x}_g = A_g e^{i\omega t}$. Therefore, the transfer function of Eq. (3) has been derived as

$$X_d(\omega) = -\frac{(m_d + m_b)}{\left[-\omega^2(m_d + m_b) + i\omega\Xi(\omega) + k_d\right]}A_g \tag{4}$$

The frequency domain function of $\Xi(\omega)$, i.e., $\Xi(\omega) = k_v c_d/(i\omega c_d + k_v)$ has been substituted in Eq. (4). Thereofore, the modified version of Eq. (4) has been expressed as

$$X_d(\omega) = -\frac{(m_d + m_b)}{\left[-\omega^2(m_d + m_b) + \frac{i\omega k_v c_d}{i\omega c_d + k_v} + k_d\right]}A_g \tag{5}$$

Now, the additional inerter-based viscoelastic mass dampers are installed at the top of a single degree of freedom systems to mitigate their dynamic responses subjected to base excitations. Newton's second law has been applied to derive the governing equations of motion for the single degree of freedom system controlled by the additional inerter-based viscoelastic mass dampers

(AIVMD). The governing equations of motion for the SDOF system equipped with additional inerter-based viscoelastic mass dampers (AIVMD) have been derived and expressed as

$$\begin{aligned}(m_d+m_b)\ddot{x}_d+\int_{-\infty}^{t}\Xi(t-\tau)\dot{x}_d(\tau)d\tau+k_dx_d+m_d\ddot{x}_s&=-m_d\,\ddot{x}_g\\ m_s\ddot{x}_s+c_s\dot{x}_s+k_sx_s-\int_{-\infty}^{t}\Xi(t-\tau)\dot{x}_d(\tau)d\tau-k_dx_d&=-m_s\,\ddot{x}_g\end{aligned}\tag{6}$$

$\Xi(t-\tau)$ function has been derived and substitutes in Eq. (6). Therefore, Eq. (6) has been re-written as

$$\begin{aligned}(m_d+m_b)\ddot{x}_d+\int_{0}^{\infty}k_ve^{-(k_v/c_d)(t-\tau)}\dot{x}_d(\tau)\;d\tau+k_dx_d+m_d\ddot{x}_s&=-m_d\,\ddot{x}_g\\ m_s\ddot{x}_s+c_s\dot{x}_s+k_sx_s-\int_{0}^{\infty}k_ve^{-(k_v/c_d)(t-\tau)}\dot{x}_d(\tau)\;d\tau-k_dx_d&=-m_s\,\ddot{x}_g\end{aligned}\tag{7}$$

where $x_d(t)$ and $x_s(t)$ denote the relative lateral dynamic responses of the damper and the SDOF system, which is a function of time and drive as $x_d = u_d - u_s$ and $x_s = u_s - x_g$. The steady-state solutions for the above governing equations of motion have been derived for harmonic excitation and can be expressed as $x_d = X_de^{i\omega t}$ and $x_s = X_se^{i\omega t}$. The steady-state solutions substitute in Eq. (7) and the transfer function has been derived as

$$\begin{bmatrix}2\;q\zeta_s\omega_s+q^2+{\omega_s}^2 & -\dfrac{2{\omega_d}^2(\mu_d+\mu_b)\left(q(\alpha+1)\zeta_d+1/2\;\alpha\;\omega_d\right)}{\alpha\;\omega_d+2\;q\zeta_d}\\ \mu_dq^2 & \dfrac{2(\mu_d+\mu_b)\left(q^3\zeta_d+1/2\;q^2\omega_d\alpha+{\omega_d}^2\zeta_d\;(\alpha+1)q+1/2\;{\omega_d}^3\alpha\right)}{\alpha\;\omega_d+2\;q\zeta_d}\end{bmatrix}\begin{Bmatrix}X_s\\X_d\end{Bmatrix}=-\begin{bmatrix}1\\\mu_d\end{bmatrix}A_g\tag{8}$$

where $\alpha = k_v/k_d$, denotes the ratio of stiffness of viscoelastic material to the damper. $\mu_d = m_d/m_s$ and $\mu_b = m_b/m_s$ are representing the mass ratio of damper and inerter to the primary structure. $q = i\omega$ represents the multiplication of the unit imaginary number (i.e., $i = \sqrt{-1}$ and the excitation frequency ω. The dynamic response of the primary structure has been derived as

$$H_s(q)=\frac{X_s}{A_g}=\frac{\begin{array}{c}-2\;\alpha\;q{\omega_d}^2\zeta_d\;\mu_d-2\;\alpha\;q{\omega_d}^2\zeta_d-{\omega_d}^3\alpha\;\mu_d\\ -2\;q{\omega_d}^2\zeta_d\;\mu_d-\omega_dq^2\alpha-{\omega_d}^3\alpha-2\;\zeta_d\;q^3-2\;{\omega_d}^2\zeta_d\;q\end{array}}{\Delta}\tag{9}$$

The dynamic response of AIVMD has been derived as

$$H_d(q)=\frac{X_d}{A_g}=\frac{-\mu_d(\alpha\;\omega_d+2\;q\zeta_d)\omega_s(2\;q\zeta_s+\omega_s)}{\Delta}\tag{10}$$

Δ has been derived as

$$\begin{aligned}\Delta=\;&2\;\zeta_d\;q^5+(4\;\zeta_d\;\zeta_s\omega_s+\alpha\;\omega_d)q^4\\ &+\begin{pmatrix}2\;\alpha\;{\omega_d}^2\zeta_d\;\mu_d+2\;\alpha\;{\omega_d}^2\zeta_d+2\;\alpha\;\zeta_s\omega_s\omega_d\\ +2\;{\omega_d}^2\zeta_d\;\mu_d+2\;{\omega_d}^2\zeta_d+2\;\zeta_d\;{\omega_s}^2\end{pmatrix}q^3\\ &+\begin{pmatrix}4\;\alpha\;{\omega_d}^2\zeta_d\;\zeta_s\omega_s+{\omega_d}^3\alpha\;\mu_d+4\;{\omega_d}^2\zeta_d\;\zeta_s\omega_s\\ +{\omega_d}^3\alpha+\alpha\;\omega_d{\omega_s}^2\end{pmatrix}q^2\\ &+\left(2\;\alpha\;{\omega_d}^3\zeta_s\omega_s+2\;\alpha\;{\omega_d}^2\zeta_d\;{\omega_s}^2+2\;{\omega_d}^2\zeta_d\;{\omega_s}^2\right)q\\ &+{\omega_s}^2{\omega_d}^3\alpha\end{aligned}\tag{11}$$

Equations (9) and (11) are applied to derive the standard deviation and the corresponding closed-form expressions for optimal design parameters of AIVMD.

2.2. Additional viscoelastic mass damper inerters

Newton's second law has been applied to derive the governing equations of motion for the single degree of freedom system controlled by the additional viscoelastic mass damper inerters (AVMDI). The equations of motion of a single degree of freedom system equipped with additional viscoelastic mass damper inerters are derived and expressed as

$$\begin{aligned}(m_d+m_b)\ddot{x}_d+\int_{-\infty}^{t}\Xi(t-\tau)\dot{x}_d(\tau)d\tau+k_dx_d+(m_d+m_b)\ddot{x}_s&=-m_d\ddot{x}_g\\ m_s\ddot{x}_s+c_s\dot{x}_s+k_sx_s-\int_{-\infty}^{t}\Xi(t-\tau)\dot{x}_d(\tau)d\tau-k_dx_d&=-m_s\ddot{x}_g\end{aligned}\tag{12}$$

$\Xi(t-\tau)$ derives for viscoelastic material, followed by the standard linear solid model and substitutes in Eq. (12). Therefore, Eq. (12) has been re-written as

$$\begin{aligned}(m_d+m_b)\ddot{x}_d+\int_{0}^{\infty}k_ve^{-(k_v/c_d)(t-\tau)}\dot{x}_d(\tau)\ d\tau+k_dx_d+(m_d+m_b)\ddot{x}_s&=-m_d\ddot{x}_g\\ m_s\ddot{x}_s+c_s\dot{x}_s+k_sx_s-\int_{0}^{\infty}k_ve^{-(k_v/c_d)(t-\tau)}\dot{x}_d(\tau)\ d\tau-k_dx_d&=-m_s\ddot{x}_g\end{aligned}\tag{13}$$

As the controlled structures are subjected to harmonic excitation. Therefore, the steady-state solutions are derived as $x_d=X_de^{i\omega t}$ and $x_s=X_se^{i\omega t}$. $x_s=u_s-x_g$ and $x_d=u_d-u_s$ refer to the relative dynamic responses of primary structure and the novel damper. These harmonic solutions are substituted in Eq. (13), leading to the transfer function from where the dynamic responses of the primary structure and the damper have been derived analytically and expressed as

$$\begin{bmatrix}2\ q\zeta_s\omega_s+q^2+{\omega_s}^2 & -\dfrac{2{\omega_d}^2\left(q(\alpha+1)\zeta_d+1/2\ \alpha\ \omega_d\right)(\mu_d+\mu_b)}{\alpha\ \omega_d+2\ q\zeta_d}\\ (\mu_d+\mu_b)q^2 & \dfrac{2(\mu_d+\mu_b)\left(q^3\zeta_d+1/2\ q^2\omega_d\alpha+{\omega_d}^2\zeta_d\ (\alpha+1)q+1/2\ {\omega_d}^3\alpha\right)}{\alpha\ \omega_d+2\ q\zeta_d}\end{bmatrix}\begin{Bmatrix}X_s\\X_d\end{Bmatrix}=-\begin{bmatrix}1\\\mu_d\end{bmatrix}A_g\tag{14}$$

where $\alpha=k_v/k_d$, representing the stiffness ratio of viscoelastic material to the proposed damper. $\mu_d=m_d/m_s$ denotes the mass ratio of the damper to the primary structure. $\mu_b=m_b/m_s$ denotes the mass ratio of the inerter to the primary structure. $q=i\omega$, where i and ω represent unit imaginary number (i.e., $i=\sqrt{-1}$ and the excitation frequency. The dynamic response of the primary structure has been derived as

$$H_s(q)=\frac{X_s}{A_g}=\frac{\begin{matrix}-2\ q\alpha\ {\omega_d}^2\zeta_d\ \mu_d-2\ q\alpha\ {\omega_d}^2\zeta_d-\alpha\ {\omega_d}^3\mu_d-2\ q{\omega_d}^2\zeta_d\ \mu_d\\ -\omega_dq^2\alpha-{\omega_d}^3\alpha-2\ \zeta_d\ q^3-2\ \zeta_d\ {\omega_d}^2q\end{matrix}}{\Delta}\tag{15}$$

The dynamic response of AVMDI has been derived as

$$H_d(q) = \frac{X_d}{A_g} = \frac{(\alpha\ \omega_d + 2\ q\zeta_d)\left(-2\ q\zeta_s\mu_d\omega_s + q^2\mu_b - \mu_d{\omega_s}^2\right)}{\Delta} \tag{16}$$

Δ has been derived as

$$\begin{aligned}\Delta = {} & 2\ \zeta_d\ q^5 + (4\ \zeta_d\ \zeta_s\omega_s + \alpha\ \omega_d)q^4 \\ & + \begin{pmatrix} 2\ \alpha\ {\omega_d}^2\zeta_d\ \mu_b + 2\ \alpha\ {\omega_d}^2\zeta_d\ \mu_d + 2\ \alpha\ {\omega_d}^2\zeta_d \\ +2\ \alpha\ \zeta_s\omega_s\omega_d + 2\ {\omega_d}^2\zeta_d\ \mu_b + 2\ {\omega_d}^2\zeta_d\ \mu_d \\ +2\ \zeta_d\ {\omega_d}^2 + 2\ \zeta_d\ {\omega_s}^2 \end{pmatrix} q^3 \\ & + \begin{pmatrix} 4\ \alpha\ {\omega_d}^2\zeta_d\ \zeta_s\omega_s + \alpha\ {\omega_d}^3\mu_b + \alpha\ {\omega_d}^3\mu_d \\ +4\ {\omega_d}^2\zeta_d\ \zeta_s\omega_s + {\omega_d}^3\alpha + \alpha\ \omega_d{\omega_s}^2 \end{pmatrix} q^2 \\ & + \left(2\ \alpha\ {\omega_d}^3\zeta_s\omega_s + 2\ \alpha\ {\omega_d}^2\zeta_d\ {\omega_s}^2 + 2\ {\omega_d}^2\zeta_d\ {\omega_s}^2\right)q \\ & + {\omega_s}^2{\omega_d}^3\alpha \end{aligned} \tag{17}$$

Equations (15) and (17) utilize to determine the standard deviation (SD) and the exact closed-form expressions for the optimal design parameters for AVMDI analytically.

3. H_2 optimization

H_2 optimization method applies to analytically derive the exact mathematical formulations in terms of closed-form expressions for the optimal design parameters, such as frequency and damping ratio of AIVMD and AVMDI subjected to random-white noise excitation. Additionally, the standard deviation of the dynamic responses of the single degree of freedom systems controlled by AIVMD and AVMDI has been minimized using this optimization method.

3.1. Additional inerter-based viscoelastic mass dampers

H_2 optimization method applies to derive the exact closed-form expressions for optimal design parameters for additional inerter-based viscoelastic mass dampers (Chowdhury, Banerjee, and Adhikari 2022b; Chowdhury and Banerjee 2022b) subjected to random-white noise excitations, and in addition, $\zeta_s = 0$ considers. The mathematical expressions for determining the standard deviation (Roberts and Spanos 2003) of the dynamic responses of controlled structures are derived and expressed as

$$\sigma^2_{x_{s,d}} = \int_{-\infty}^{\infty} \frac{\Xi_n(\omega)\,\mathrm{d}\omega}{\Lambda_n(\mathrm{i}\omega)\Lambda_n^*(\mathrm{i}\omega)} = \frac{\pi}{a_5}\frac{\det[\mathbf{N}_5]}{\det[\mathbf{D}_5]} \tag{18}$$

$$N_4 = \begin{bmatrix} b_4 & b_3 & b_2 & b_1 & b_0 \\ -a_5 & a_3 & -a_1 & 0 & 0 \\ 0 & -a_4 & a_2 & -a_0 & 0 \\ 0 & a_5 & -a_3 & a_1 & 0 \\ 0 & 0 & a_4 & -a_2 & a_0 \end{bmatrix} \quad \text{and} \quad D_4 = \begin{bmatrix} a_4 & -a_2 & a_0 & 0 & 0 \\ -a_5 & a_3 & -a_1 & 0 & 0 \\ 0 & -a_4 & a_2 & -a_0 & 0 \\ 0 & a_5 & -a_3 & a_1 & 0 \\ 0 & 0 & a_4 & -a_2 & a_0 \end{bmatrix} \tag{19}$$

Equations (9) and (11) are substituted in Eqs. (18) and (19). Therefore, the SD of the dynamic response of the primary structure derives as

$$\sigma_{x_s}^2 = \frac{S_0\pi \begin{pmatrix} 4\ \omega_s^2\omega_d^4\alpha^2\zeta_d^2\mu_d^3 + \alpha^2\omega_d^6\mu_d^4 + 12\ \omega_s^2\omega_d^4\alpha^2\zeta_d^2\mu_d^2 - 8\ \omega_d^2\zeta_d^2\omega_s^4 \\ +8\ \omega_s^2\omega_d^4\alpha\ \zeta_d^2\mu_d^3 + 4\ \alpha^2\omega_d^6\mu_d^3 + 12\ \omega_s^2\omega_d^4\alpha^2\zeta_d^2\mu_d + \omega_s^2\omega_d^4\alpha^2\mu_d^3 \\ +24\ \omega_s^2\omega_d^4\alpha\ \zeta_d^2\mu_d^2 + 4\ \omega_s^2\omega_d^4\zeta_d^2\mu_d^3 + 6\ \alpha^2\omega_d^6\mu_d^2 + 4\ \omega_s^2\omega_d^4\alpha^2\zeta_d^2 \\ +24\ \omega_s^2\omega_d^4\zeta_d^2\alpha\ \mu_d - 8\ \alpha\ \omega_d^2\zeta_d^2\mu_d\omega_s^4 + 12\ \omega_s^2\omega_d^4\zeta_d^2\mu_d^2 + 4\ \alpha^2\omega_d^6\mu_d \\ +8\ \omega_s^2\omega_d^4\alpha\ \zeta_d^2 - 8\ \alpha\ \omega_d^2\zeta_d^2\omega_s^4 + 12\ \omega_s^2\omega_d^4\zeta_d^2\mu_d - 8\ \omega_d^2\zeta_d^2\mu_d\omega_s^4 \\ +\alpha^2\omega_d^6 - 2\ \omega_s^2\omega_d^4\alpha^2 + \alpha^2\omega_d^2\omega_s^4 - 3\ \omega_s^2\omega_d^4\alpha^2\mu_d + 4\ \omega_s^2\omega_d^4\zeta_d^2 + 4\ \zeta_d^2\omega_s^6 \end{pmatrix}}{2\ \alpha^2\omega_d^3\zeta_d\ \mu_d\omega_s^6} \tag{20}$$

Equation (20) partially differentiates w.r.t the viscous damping ratio ζ_d and the natural frequency ω_d of AIVMD. Therefore, the mathematical expressions are derived as follows,

$$\frac{\partial\sigma_{x_s}^2}{\partial\zeta_d} = 0 \quad \text{and} \quad \frac{\partial\sigma_{x_s}^2}{\partial\omega_d} = 0 \tag{21}$$

Equation (20) substitutes in the first expression of Equation (21). Correspondingly, the exact closed-form expression for the viscous damping ratio of AIVMD derives as

$$(\zeta_d)_{opt} = \sqrt{\frac{\left((\mu_d+1)^4w^4 + \omega_s^2(\mu_d-2)(\mu_d+1)^2w^2 + \omega_s^4\right)\alpha^2w^2}{4\ \omega_s^2\left((\mu_d+1)^3(\alpha+1)^2w^4 - 2\ \omega_s^2(\mu_d+1)(\alpha+1)w^2 + \omega_s^4\right)}} \tag{22}$$

Equation (22) contains the optimal natural frequency of the AIVMD, which needs to be subtracted. To perform that, Eq. (22) substitutes in Eq. (20). Accordingly, the modified SD for the dynamic response of the primary structure derives as

$$\sigma_{x_s}^2 = \frac{2S_0\pi\ \left((\mu_d+1)^4\omega_d^4 + \omega_s^2(\mu_d-2)(\mu_d+1)^2\omega_d^2 + \omega_s^4\right)}{\sqrt{\frac{\alpha^2\omega_d^2\left((\mu_d+1)^4\omega_d^4+\omega_s^2(\mu_d-2)(\mu_d+1)^2\omega_d^2+\omega_s^4\right)}{\left((\mu_d+1)^3(\alpha+1)^2\omega_d^4-2\ \omega_s^2(\mu_d+1)(\alpha+1)\omega_d^2+\omega_s^4\right)\omega_s^2}\omega_d\mu_d\omega_s^6}} \tag{23}$$

Equation (23) replaces in the second expression of Eq. (21). As a result, the exact closed-form expression for the optimal frequency of AIVMD derives as

$$\begin{gathered} 2\ (\mu_d+1)^7(\alpha+1)^2\omega_d^8 + (\alpha+1)\left((\alpha+1)\mu_d - 2\ \alpha - 4\right)(\mu_d+1)^5\omega_s^2\omega_d^6 \\ +2\ \left(-1/2\ \mu_d^2 + \alpha + 1/2\ \mu_d + 2\right)(\mu_d+1)\omega_s^6\omega_d^2 - 2\ \omega_s^8 = 0 \\ (\omega_d)_{opt} = \frac{\sqrt{2}}{4}\sqrt{\frac{\left((\alpha+1)\mu_d - 2\ \alpha - 4\right)\omega_s^2}{(\mu_d+1)^2(\alpha+1)}} \quad \text{and} \quad (\eta_d)_{opt} = \frac{\sqrt{2}}{4}\sqrt{\frac{\left((\alpha+1)\mu_d - 2\ \alpha - 4\right)}{(\mu_d+1)^2(\alpha+1)}} \end{gathered} \tag{24}$$

Equation (24) substitutes in Eq. (22), and the optimal viscous damping ratio for AIVMD determines eventually. The variations of the optimal frequency ratio of AIVMD versus damper mass ratio are shown in Fig. 2(a). Equation (24) applies for Fig. 2(a) and $\alpha = 1.0$ considers for this figure. The optimal frequency ratio of AIVMD decreases as the damper mass ratio increases. The effect of the damper mass ratio on the optimal viscous damping ratio of AIVMD has also been investigated. Accordingly, the variations of the optimal viscous damping ratio of AIVMD versus damper mass ratio are shown in Fig. 2(b). Equation (22) and $\alpha = 1.0$ implement for Fig. 2(b). The optimal viscous damping ratio of AIVMD decreases as the damper mass ratio increases. Hence, a higher damper mass ratio recommends achieving the robust vibration reduction capacity for optimum AIVMD with moderate frequency and lower viscous damping ratios at affordable ranges.

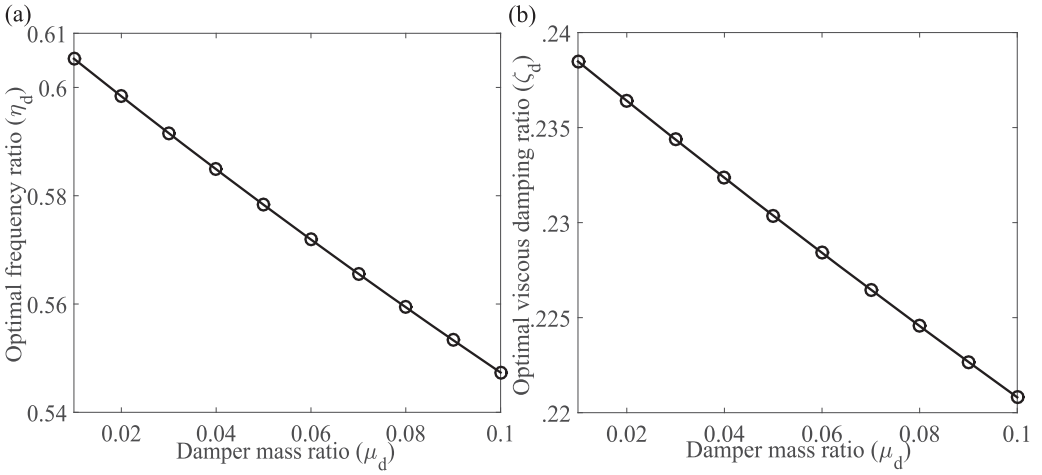

Figure 2. The variations of optimal (a) frequency ratio and (b) viscous damping ratio of AIVMD versus damper mass ratio.

3.2. Additional viscoelastic mass damper inerters

Equations (15) and (17) are substituted in Eqs. (18) and (19). Therefore, the standard deviation (SD) of the dynamic response of the primary structure controlled by AVMDI has been derived as

$$\sigma_{x_s}^2 = \frac{S_0\pi \begin{pmatrix} 4\ \alpha^2\zeta_d{}^2\mu_b\mu_d{}^2\omega_d{}^4\omega_s{}^2 + 4\ \alpha^2\zeta_d{}^2\mu_d{}^3\omega_d{}^4\omega_s{}^2 - 8\ \zeta_d{}^2\omega_d{}^2\omega_s{}^4 \\ +12\ \alpha^2\zeta_d{}^2\mu_d{}^2\omega_d{}^4\omega_s{}^2 + \alpha^2\mu_b{}^2\mu_d{}^2\omega_d{}^6 + 2\ \alpha^2\mu_b\mu_d{}^3\omega_d{}^6 \\ +\alpha^2\mu_d{}^4\omega_d{}^6 + 8\ \alpha\ \zeta_d{}^2\mu_b\mu_d{}^2\omega_d{}^4\omega_s{}^2 + 8\ \alpha\ \zeta_d{}^2\mu_d{}^3\omega_d{}^4\omega_s{}^2 \\ +4\ \alpha^2\zeta_d{}^2\mu_b\omega_d{}^4\omega_s{}^2 + 12\ \alpha^2\zeta_d{}^2\mu_d\omega_d{}^4\omega_s{}^2 + 2\ \alpha^2\mu_b{}^2\mu_d\omega_d{}^6 \\ +6\ \alpha^2\mu_b\mu_d{}^2\omega_d{}^6 + \alpha^2\mu_b\mu_d{}^2\omega_d{}^4\omega_s{}^2 + 4\ \alpha^2\mu_d{}^3\omega_d{}^6 \\ +\alpha^2\mu_d{}^3\omega_d{}^4\omega_s{}^2 + 16\ \alpha\ \zeta_d{}^2\mu_b\mu_d\omega_d{}^4\omega_s{}^2 + 24\ \alpha\ \zeta_d{}^2\mu_d{}^2\omega_d{}^4\omega_s{}^2 \\ +4\ \zeta_d{}^2\mu_b\mu_d{}^2\omega_d{}^4\omega_s{}^2 + 4\ \zeta_d{}^2\mu_d{}^3\omega_d{}^4\omega_s{}^2 + 4\ \alpha^2\zeta_d{}^2\omega_d{}^4\omega_s{}^2 \\ +\alpha^2\mu_b{}^2\omega_d{}^6 + 6\ \alpha^2\mu_b\mu_d\omega_d{}^6 + 6\ \alpha^2\mu_d{}^2\omega_d{}^6 + 8\ \alpha\ \zeta_d{}^2\mu_b\omega_d{}^4\omega_s{}^2 \\ +24\ \alpha\ \zeta_d{}^2\mu_d\omega_d{}^4\omega_s{}^2 - 8\ \alpha\ \zeta_d{}^2\mu_d\omega_d{}^2\omega_s{}^4 + 8\ \zeta_d{}^2\mu_d\omega_d{}^4\mu_b\omega_s{}^2 \\ +12\ \zeta_d{}^2\mu_d{}^2\omega_d{}^4\omega_s{}^2 + 2\ \alpha^2\mu_b\omega_d{}^6 - \alpha^2\mu_b\omega_d{}^4\omega_s{}^2 + 4\ \alpha^2\mu_d\omega_d{}^6 \\ -3\ \alpha^2\mu_d\omega_d{}^4\omega_s{}^2 + 8\ \alpha\ \zeta_d{}^2\omega_d{}^4\omega_s{}^2 - 8\ \alpha\ \zeta_d{}^2\omega_d{}^2\omega_s{}^4 \\ +4\ \zeta_d{}^2\omega_d{}^4\mu_b\omega_s{}^2 + 12\ \zeta_d{}^2\mu_d\omega_d{}^4\omega_s{}^2 - 8\ \zeta_d{}^2\mu_d\omega_d{}^2\omega_s{}^4 \\ +\alpha^2\omega_d{}^6 - 2\ \alpha^2\omega_d{}^4\omega_s{}^2 + \alpha^2\omega_d{}^2\omega_s{}^4 + 4\ \zeta_d{}^2\omega_d{}^4\omega_s{}^2 \\ +8\ \alpha^2\zeta_d{}^2\mu_b\mu_d\omega_d{}^4\omega_s{}^2 + 4\ \zeta_d{}^2\omega_s{}^6 \end{pmatrix}}{2\ \alpha^2\zeta_d\omega_d{}^3\omega_s{}^6(\mu_b+\mu_d)} \tag{25}$$

Equation (25) partially differentiates w.r.t the viscous damping ratio ζ_d and natural frequency ω_d of AVMDI. The mathematical expressions for partial differentiation are derived as

$$\frac{\partial\sigma_{x_s}^2}{\partial\zeta_d} = 0 \quad \text{and} \quad \frac{\partial\sigma_{x_s}^2}{\partial\omega_d} = 0 \tag{26}$$

Equation (25) has been substituted in the first equation of Eq. (26). As a result, the closed-form expression for the viscous damping ratio of AVMDI has been derived as

$$(\zeta_d)_{opt} = \sqrt{\frac{{\omega_d}^2\begin{pmatrix}(\mu_d+1)^2(\mu_b+\mu_d+1)^2{\omega_d}^4+{\omega_s}^4\\+{\omega_s}^2\left({\mu_d}^2+(\mu_b-1)\mu_d-\mu_b-2\right)(\mu_d+1){\omega_d}^2\end{pmatrix}\alpha^2}{4\ {\omega_s}^2\begin{pmatrix}(\mu_d+1)^2(\alpha+1)^2(\mu_b+\mu_d+1){\omega_d}^4\\-2\ {\omega_s}^2(\mu_d+1)(\alpha+1){\omega_d}^2+{\omega_s}^4\end{pmatrix}}} \tag{27}$$

The optimal frequency of AVMDI needs to be separated from Eq. (22) to achieve the exact closed-form expression for AVMDI. To perform that Eq. (27) has been substituted in Eq. (25). The modified SD of the dynamic response of the primary structure derives as

$$\sigma_{x_s}^2 = \frac{2S_0\pi\begin{pmatrix}(\mu_d+1)^2(\mu_b+\mu_d+1)^2{\omega_d}^4+{\omega_s}^4\\+(\mu_d+1){\omega_s}^2\left({\mu_d}^2+(\mu_b-1)\mu_d-\mu_b-2\right){\omega_d}^2\end{pmatrix}}{\omega_d{\omega_s}^6(\mu_b+\mu_d)\sqrt{\frac{{\omega_d}^2\begin{pmatrix}(\mu_d+1)^2(\mu_b+\mu_d+1)^2{\omega_d}^4+{\omega_s}^4\\+(\mu_d+1){\omega_s}^2\left({\mu_d}^2+(\mu_b-1)\mu_d-\mu_b-2\right){\omega_d}^2\end{pmatrix}^{\alpha^2}}{{\omega_s}^2\begin{pmatrix}(\mu_d+1)^2(\alpha+1)^2(\mu_b+\mu_d+1){\omega_d}^4\\-2\ (\mu_d+1){\omega_s}^2(\alpha+1){\omega_d}^2+{\omega_s}^4\end{pmatrix}}}} \tag{28}$$

Equation (28) substitutes in the second equation of Eq. (26). The closed-form expression for the optimal frequency of AVMDI has been derived as

$$\begin{gathered}2\ (\mu_d+1)^4(\mu_b+\mu_d+1)^3(\alpha+1)^2{\omega_d}^8\\+\left((\alpha+1){\mu_d}^2+((\mu_b-1)\alpha+\mu_b-3)\mu_d+(-\mu_b-2)\alpha-3\ \mu_b-4\right)\\(\alpha+1){\omega_s}^2(\mu_d+1)^3(\mu_b+\mu_d+1){\omega_d}^6\\+2\ \left(-1/2\ {\mu_d}^2+(-1/2\ \mu_b+1/2)\mu_d+\alpha+1/2\ \mu_b+2\right){\omega_s}^6(\mu_d+1){\omega_d}^2-2\ {\omega_s}^8\end{gathered} = 0$$

$$(\omega_d)_{opt} = \frac{\sqrt{2}}{4}\sqrt{\frac{\left(\left({\mu_d}^2+(\mu_b-1)\mu_d-\mu_b-2\right)\alpha+{\mu_d}^2+(\mu_b-3)\mu_d-3\ \mu_b-4\right){\omega_s}^2}{(\alpha+1)(\mu_d+1)(\mu_b+\mu_d+1)^2}} \tag{29}$$

$$(\eta_d)_{opt} = \frac{\sqrt{2}}{4}\sqrt{\frac{\left(\left({\mu_d}^2+(\mu_b-1)\mu_d-\mu_b-2\right)\alpha+{\mu_d}^2+(\mu_b-3)\mu_d-3\ \mu_b-4\right)}{(\alpha+1)(\mu_d+1)(\mu_b+\mu_d+1)^2}}$$

The variations of the optimal frequency ratio of AVMDI versus damper mass ratio for different values of inerter mass ratio have been shown in Fig. 3(a). Equation (29) and $\alpha = 1.0$ are applied for this figure. The optimal frequency ratio decreases when the damper and inerter mass ratios increase. The variations of the optimal viscous damping ratio of AVMDI versus damper mass ratio for different values of inerter mass ratio have been shown in Fig. 3(b). Equation (27) and $\alpha = 1.0$ are applied for this figure. The optimal viscous damping ratio decreases when the damper and inerter mass ratios increase. According to the parametric study, for achieving optimum dynamic response reduction capacity from AVMDI, a higher damper mass ratio and a higher inerter mass ratio recommend. Applying one of the above-determined optimal design parameters for optimum AVMDI, the variations of the optimal dynamic response graphs are determined for SODF systems controlled by AIVMD and AVMDI. Precisely, the variations of the optimal dynamic responses of the primary structures controlled by H_2 optimized AIVMD versus frequency ratio for different values of viscous damping ratios of the dampers are shown in Fig. 4(a). The system parameters are utilized for this figure are $\mu_d = 0.04$, $\mu_b = 0.01$, and $\alpha = 1.0$. These parameters are substituted in Eqs. (24) and (22), and the optimal frequency and damping ratios are obtained at 0.5849 and 0.2324. At $\zeta_d = 0$, the controlled dynamic systems are oscillating to their eigen frequencies, i.e., $\eta = 0.579$ and $\eta = 1.01$. The frequency points are shifted from these eigen frequencies at $\zeta_d > 0$. At $(\zeta_d)_{opt} = 0.2324$, the resonance occurs, and the maximum displacement of the primary structure minimizes effectively. The resonating frequencies are

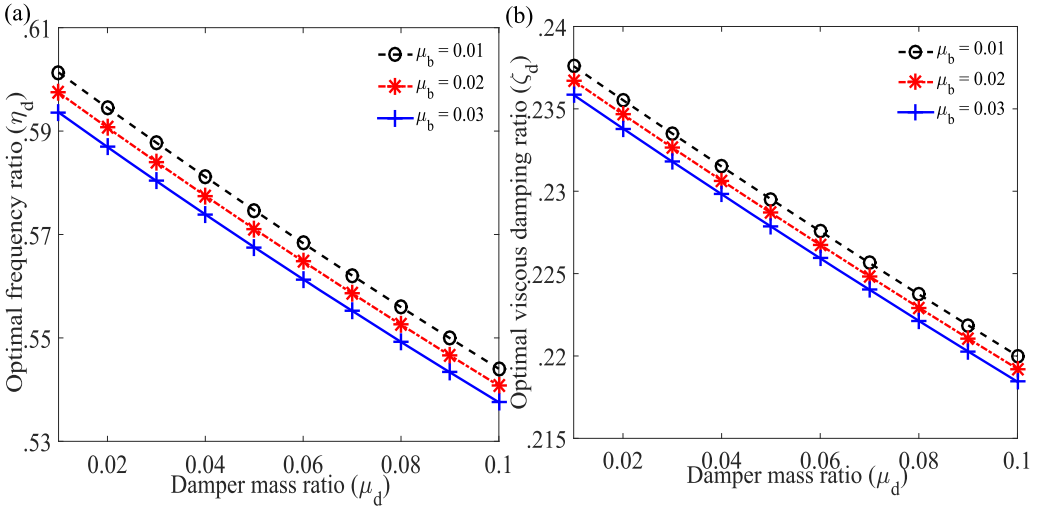

Figure 3. The variations of optimal (a) frequency ratio and (b) viscous damping ratio of AVMDI versus damper mass ratio for different values of inerter mass ratio.

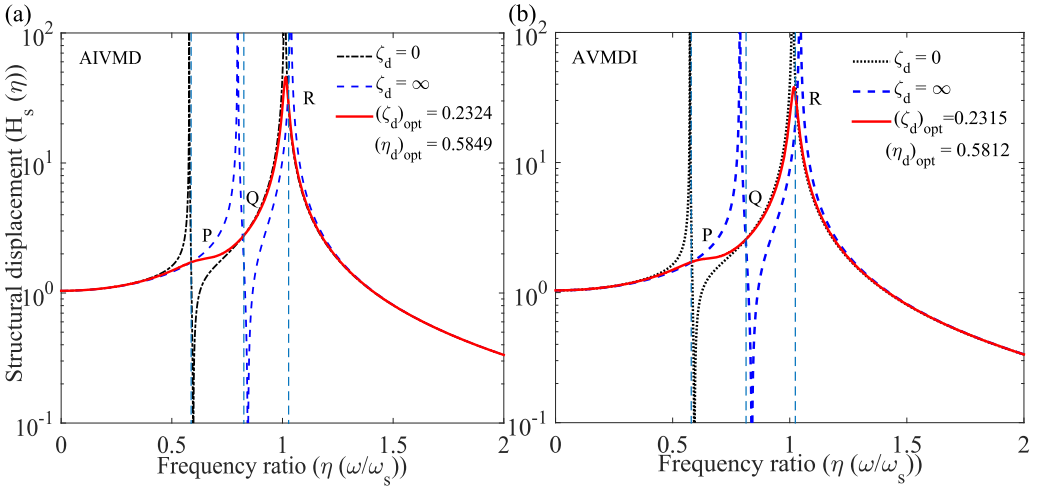

Figure 4. The variations of optimal dynamic responses of primary structure controlled by (a) AIVMD, (b) AVMDI versus frequency ratio for different values of viscous damping ratios of the dampers.

obtained at $\eta = 0.6003$ and $\eta = 1.015$. After increasing $\zeta_d > (\zeta_d)_{opt}$, the dynamic responses are slightly increases and massively increases at $\zeta_d = \infty$. Two frequency points are located at $\eta = 0.7977$ and $\eta = 1.037$. The optimal performance of optimal design parameters for AVMDI has also been investigated through optimal dynamic response plots. Therefore, the differences in responses of the main structures equipped H_2 optimized AVMDI with frequency ratio to the different values of damping ratios are displayed in Fig. 4(b). $\mu_d = 0.04$, $\mu_b = 0.01$, and $\alpha = 1.0$ are selected for this graph and also applied to Eqs. (29) and (27). The optimal frequency and damping ratios are obtained at $\eta_d = 0.5812$ and $\zeta_d = 0.2315$. $\eta = 0.574$ and $\eta = 1.013$ are the eigen frequencies at $\zeta_d = 0$ which are shifted to $\eta = 0.5873$ and $\eta = 1.018$ at $(\zeta_d)_{opt} = 0.2315$, mentioned as the resonating frequency zones. Massive response amplifications are occurred at $\zeta_d = \infty$ and frequency regions are $\eta = 0.7876$ and $\eta = 1.044$.

4. H_∞ optimization

H_∞ optimization method applies to analytically derive the exact mathematical formulations in terms of closed-form expressions for the optimal design parameters, such as frequency and damping ratio of AIVMD and AVMDI subjected to harmonic excitation. Additionally, the dynamic responses of the single degree of freedom systems controlled by AIVMD and AVMDI have been minimized using this optimization method.

4.1. Additional inerter-based viscoelastic mass dampers

The closed-form expressions for optimal design parameters of AIVMD have also been derived through the H_∞ optimization method when the controlled structures are subjected to harmonic excitations. To perform that, the transfer function in Eq. (8) has been non-dimensionalized and expressed as

$$\begin{bmatrix} -\eta^2 + 2\ i\zeta_s\eta + 1 & \dfrac{-2\ i\eta\ \alpha\ {\eta_d}^3\zeta_d\ (\mu_d+\mu_b)^2}{\alpha\ {\eta_d}^2(\mu_d+\mu_b) + i(2\ \mu_d + 2\ \mu_b)\eta\ \zeta_d\ \eta_d} - {\eta_d}^2(\mu_d+\mu_b) \\ -\mu_d\eta^2 & A_{22} \end{bmatrix} \begin{Bmatrix} X_s \\ X_d \end{Bmatrix} = -\begin{bmatrix} 1 \\ \mu_d \end{bmatrix} \frac{A_g}{\omega_s^2}$$
$$A_{22} = -(\mu_d+\mu_b)\eta^2 + \frac{2\ i\eta\ \alpha\ {\eta_d}^3\zeta_d\ (\mu_d+\mu_b)^2}{\alpha\ {\eta_d}^2(\mu_d+\mu_b) + i(2\ \mu_d + 2\ \mu_b)\eta\ \zeta_d\ \eta_d} + {\eta_d}^2(\mu_d+\mu_b) \tag{30}$$

The dynamic response of the primary structure has been derived as

$$H_s = \frac{X_s}{A_g}\omega_s^2 = \frac{\begin{array}{c} {\eta_d}^3\alpha\ \mu_d - \eta_d\eta^2\alpha + {\eta_d}^3\alpha \\ +\mathrm{i}\left(2\ \alpha\ \eta\ {\eta_d}^2\zeta_d\ \mu_d + 2\ \alpha\ \eta\ {\eta_d}^2\zeta_d + 2\ \eta\ {\eta_d}^2\zeta_d\ \mu_d - 2\ \eta^3\zeta_d + 2\ \eta\ {\eta_d}^2\zeta_d\right) \end{array}}{\Delta} \tag{31}$$

The dynamic response of AIVMD has been derived as

$$H_d = \frac{X_d}{A_g}\omega_s^2 = \frac{-4\ \mu_d\zeta_s\eta^2\zeta_d + \mu_d\alpha\ \eta_d + \mathrm{i}(2\ \mu_d\zeta_s\eta\ \alpha\ \eta_d + 2\ \mu_d\eta\ \zeta_d)}{\Delta} \tag{32}$$

Δ has been derived as

$$\Delta = \begin{array}{c} \alpha\ \eta^2{\eta_d}^3\mu_d + 4\ \alpha\ \eta^2{\eta_d}^2\zeta_d\ \zeta_s - \alpha\ \eta^4\eta_d + \alpha\ \eta^2{\eta_d}^3 - 4\ \eta^4\zeta_d\ \zeta_s + 4\ \eta^2{\eta_d}^2\zeta_d\ \zeta_s + \eta_d\eta^2\alpha - {\eta_d}^3\alpha \\ +\mathrm{i}\left(\begin{array}{c} 2\ \alpha\ \eta^3{\eta_d}^2\zeta_d\ \mu_d + 2\ \alpha\ \eta^3{\eta_d}^2\zeta_d + 2\ \eta^3{\eta_d}^2\zeta_d\ \mu_d + 2\ \alpha\ \eta^3\eta_d\zeta_s - 2\ \alpha\ \eta\ {\eta_d}^3\zeta_s - 2\ \zeta_d\ \eta^5 \\ +2\ \eta^3{\eta_d}^2\zeta_d - 2\ \alpha\ \eta\ {\eta_d}^2\zeta_d + 2\ \eta^3\zeta_d - 2\ \eta\ {\eta_d}^2\zeta_d \end{array}\right) \end{array} \tag{33}$$

The resultant of H_s has been summarized as

$$|H_s| = \sqrt{\frac{y_1^2 + \zeta_d^2 y_2^2}{y_3^2 + \zeta_d^2 y_4^2}} = \frac{y_2}{y_4}\sqrt{\frac{\frac{y_1^2}{y_2^2} + \zeta_d^2}{\frac{y_3^2}{y_4^2} + \zeta_d^2}} \tag{34}$$

From Eq. (58), the first restraint (Den Hartog 1985) for H_∞ optimization has been derived as

$$\left|\frac{y_1}{y_2}\right| = \left|\frac{y_3}{y_4}\right| \tag{35}$$

An equation has been derived after applying Eq. (35) and expressed as

$$\begin{gathered}\eta^6+\left(-\mu_d\alpha\ {\eta_d}^2-\alpha\ {\eta_d}^2-2\ \mu_d{\eta_d}^2-2\ {\eta_d}^2-1\right)\eta^4\\+\left(\begin{gathered}{\mu_d}^2\alpha\ {\eta_d}^4+2\ \alpha\ {\eta_d}^4\mu_d+{\mu_d}^2{\eta_d}^4+\alpha\ {\eta_d}^4+2\ {\eta_d}^4\mu_d\\+1/2\ \mu_d\alpha\ {\eta_d}^2+{\eta_d}^4+\alpha\ {\eta_d}^2+\mu_d{\eta_d}^2+2\ {\eta_d}^2\\-\alpha\ {\eta_d}^4\mu_d-\alpha\ {\eta_d}^4-{\eta_d}^4\mu_d-{\eta_d}^4\end{gathered}\right)\eta^2=0\end{gathered}\tag{36}$$

Equation (36) has been summarized as

$$\eta^6+\left(-{\eta_1}^2-{\eta_2}^2-{\eta_3}^2\right)\eta^4+\left({\eta_1}^2{\eta_2}^2+{\eta_3}^2{\eta_1}^2+{\eta_2}^2{\eta_3}^2\right)\eta^2-{\eta_1}^2{\eta_2}^2{\eta_3}^2=0\tag{37}$$

Therefore, the roots for Equation (36) have been derived as

$$\begin{aligned}{\eta_1}^2+{\eta_2}^2+{\eta_3}^2&=\mu_d\alpha\ {\eta_d}^2+\alpha\ {\eta_d}^2+2\ {\eta_d}^2\mu_d+2\ {\eta_d}^2+1\\{\eta_1}^2{\eta_2}^2+{\eta_3}^2{\eta_1}^2+{\eta_2}^2{\eta_3}^2&=\begin{gathered}{\mu_d}^2\alpha\ {\eta_d}^4+2\ \alpha\ {\eta_d}^4\mu_d+{\mu_d}^2{\eta_d}^4+\alpha\ {\eta_d}^4+2\ {\eta_d}^4\mu_d\\+1/2\ \mu_d\alpha\ {\eta_d}^2+{\eta_d}^4+\alpha\ {\eta_d}^2+{\eta_d}^2\mu_d+2\ {\eta_d}^2\\\eta_1^2\eta_2^2\eta_3^2=\alpha\ {\eta_d}^4\mu_d+\alpha\ {\eta_d}^4+{\eta_d}^4\mu_d+{\eta_d}^4\end{gathered}\end{aligned}\tag{38}$$

From Eq. (58), the second constraint (Den Hartog 1985) has been derived as

$$(H_s)_{\eta_1,\eta_2}=\left|\frac{y_2}{y_4}\right|\tag{39}$$

$$\eta_1^2+\eta_2^2=0\tag{40}$$

Equation (64) substitutes in the first equation of Eq. (38). Hence, η_3^2 derives as

$${\eta_3}^2=\mu_d\alpha\ {\eta_d}^2+\alpha\ {\eta_d}^2+2\ {\eta_d}^2\mu_d+2\ {\eta_d}^2+1\tag{41}$$

Equation (41) has been substituted in the second and third equations of Equation (38). Therefore, the closed-form expressions for ${\eta_1}^2{\eta_2}^2$ have been derived as

$$\begin{aligned}{\eta_1}^2{\eta_2}^2&=\begin{gathered}{\mu_d}^2\alpha\ {\eta_d}^4+2\ \alpha\ {\eta_d}^4\mu_d+{\mu_d}^2{\eta_d}^4+\alpha\ {\eta_d}^4+2\ {\eta_d}^4\mu_d\\+1/2\ \mu_d\alpha\ {\eta_d}^2+{\eta_d}^4+\alpha\ {\eta_d}^2+{\eta_d}^2\mu_d+2\ {\eta_d}^2\\\eta_1^2\eta_2^2\eta_3^2=\alpha\ {\eta_d}^4\mu_d+\alpha\ {\eta_d}^4+{\eta_d}^4\mu_d+{\eta_d}^4\end{gathered}\end{aligned}\tag{42}$$

$${\eta_1}^2{\eta_2}^2=\frac{{\eta_d}^4(\mu_d+1)(\alpha+1)}{1+(\mu_d+1)(\alpha+2){\eta_d}^2}\tag{43}$$

Equations (42) and (43) are equated, and the closed-form expression for the optimal frequency ratio of AIVMD has been derived as

$$\begin{gathered}\left(\begin{gathered}2\ \alpha^2{\mu_d}^3+6\ \alpha^2{\mu_d}^2+6\ \alpha\ {\mu_d}^3+6\ \alpha^2\mu_d+18\ \alpha\ {\mu_d}^2+4\ {\mu_d}^3+2\ \alpha^2\\+18\ \alpha\ \mu_d+12\ {\mu_d}^2+6\ \alpha+12\ \mu_d+4\end{gathered}\right){\eta_d}^4\\+\left(\alpha^2{\mu_d}^2+3\ \alpha^2\mu_d+6\ \alpha\ {\mu_d}^2+2\ \alpha^2+14\ \alpha\ \mu_d+6\ {\mu_d}^2+8\ \alpha+14\ \mu_d+8\right){\eta_d}^2\\+\alpha\ \mu_d+2\ \alpha+2\ \mu_d+4\end{gathered}=0\tag{44}$$

$$w_2{\eta_d}^4+w_1{\eta_d}^2+w_0=0\tag{45}$$

$$(\eta_{d1})_{opt}^2=\frac{-w_1+\sqrt{{w_1}^2-4\ w_2w_0}}{2w_2}\quad\text{and}\quad(\eta_{d2})_{opt}^2=\frac{-w_1-\sqrt{{w_1}^2-4\ w_2w_0}}{2w_2}\tag{46}$$

After applying Eqs. (42) and (43), the closed-form expressions for $\eta_{1,2}^2$ are derived as

$$\eta_{1,2}^2 = \pm\sqrt{\begin{array}{c}{\mu_d}^2\alpha\ {\eta_d}^4 + 2\ \alpha\ {\eta_d}^4\mu_d + {\mu_d}^2{\eta_d}^4 + \alpha\ {\eta_d}^4 + 2\ {\eta_d}^4\mu_d \\ +1/2\ \mu_d\alpha\ {\eta_d}^2 + {\eta_d}^4 + \alpha\ {\eta_d}^2 + {\eta_d}^2\mu_d + 2\ {\eta_d}^2\end{array}} \tag{47}$$

$$\eta_{1,2}^2 = \pm\sqrt{\frac{{\eta_d}^4(\mu_d+1)(\alpha+1)}{1+(\mu_d+1)(\alpha+2){\eta_d}^2}} \tag{48}$$

The mathematical expressions for determining the closed-form expression for the optimal viscous damping ratio of AIVMD have been derived as

$$\left.\frac{\partial|H_s(\eta)|^2}{\partial\eta^2}\right|_{\eta_{1,2}^2} = 0 \quad \text{and} \quad (\zeta_d)_{opt} = \sqrt{\frac{\zeta_{d1}^2+\zeta_{d2}^2}{2}} \tag{49}$$

Therefore, the closed-form expression for the optimal viscous damping ratio of AIVMD has been derived as

$$z_2\zeta_d^4 + z_1\zeta_d^2 + z_0 = 0 \quad \text{and} \quad \zeta_{d1,d2}^2 = \frac{-z_1 \pm \sqrt{-4\ z_2z_0 + {z_1}^2}}{2z_2} \tag{50}$$

The closed-form expressions for z_2, z_1, and z_0 have been derived as

$$z_2 = \begin{array}{c}-32\ \left(-(\mu_d+1)(\alpha+1){\eta_{d1,d2}}^2 + \eta_{1,2}^2\right) \\ \left(-(\alpha+1)\left(\eta_{1,2}^2\mu_d + \eta_{1,2}^2 - 1\right){\eta_{d1,d2}}^2 + {\eta_{1,2}^2}^2 - \eta_{1,2}^2\right)\eta_{1,2}^4 \\ \left((\mu_d+1)^2(\alpha+1)^2{\eta_{d1,d2}}^4 - 2\ (\alpha+1)\left(\left(\eta_{1,2}^2 - 1/2\right)\mu_d + \eta_{1,2}^2\right){\eta_{d1,d2}}^2 + \eta_{1,2}^4\right)\end{array} \tag{51}$$

$$z_1 = -16\begin{pmatrix} (\mu_d+1)^3\left(-1+(\mu_d+1)\eta_{1,2}^2\right)(\alpha+1)^2w^8 \\ -2\ (\mu_d+1)(\alpha+1)\begin{pmatrix}(\mu_d+1)^2(\alpha+2)\eta_{1,2}^4 + 1/2\ \mu_d \\ -1/4\ (\mu_d+1)\left((\alpha+4)\mu_d + 4\ \alpha + 8\right)\eta_{1,2}^2\end{pmatrix}{\eta_{d1,d2}}^6 \\ +\left((\mu_d+1)\eta_{1,2}^2 - 1/2\ \mu_d - 1\right) \\ \left((\alpha^2+6\ \alpha+6)(\mu_d+1)\eta_{1,2}^2 - 1/2\ \mu_d(\alpha^2+2\ \alpha+4)\right)\eta_{1,2}^2\eta_{d1,d2}^4 \\ -2\begin{pmatrix}(\mu_d+1)(\alpha+2)\eta_{1,2}^4 + 1/2\ \mu_d \\ +\left((-3/4\ \alpha-2)\mu_d - \alpha - 2\right)\eta_{1,2}^2\end{pmatrix}{\eta_{1,2}^2}^2{\eta_{d1,d2}}^2 + \eta_{1,2}^8\left(\eta_{1,2}^2-1\right) \\ \alpha^2\eta_{1,2}^2{\eta_{d1,d2}}^2 \end{pmatrix} \tag{52}$$

$$z_0 = \begin{array}{c}-2\ \left((\mu_d+1)^2{\eta_{d1,d2}}^4 + \left((-2\ \mu_d-2)\eta_{1,2}^2 + \mu_d\right){\eta_{d1,d2}}^2 + \eta_{1,2}^4\right){\eta_{d1,d2}}^4 \\ \left((-\mu_d-1){\eta_{d1,d2}}^2 + \eta_{1,2}^2\right) \\ \left(\left(1+(-\mu_d-1)\eta_{1,2}^2\right){\eta_{d1,d2}}^2 + \eta_{1,2}^4 - \eta_{1,2}^2\right)\alpha^4\end{array} \tag{53}$$

The variations of the optimal frequency ratio of the AIVMD versus damper mass ratio are shown in Fig. 5(a). $\alpha = 1.0$ is accounted for in this graph. Equation (46) contains two exact closed-form expressions

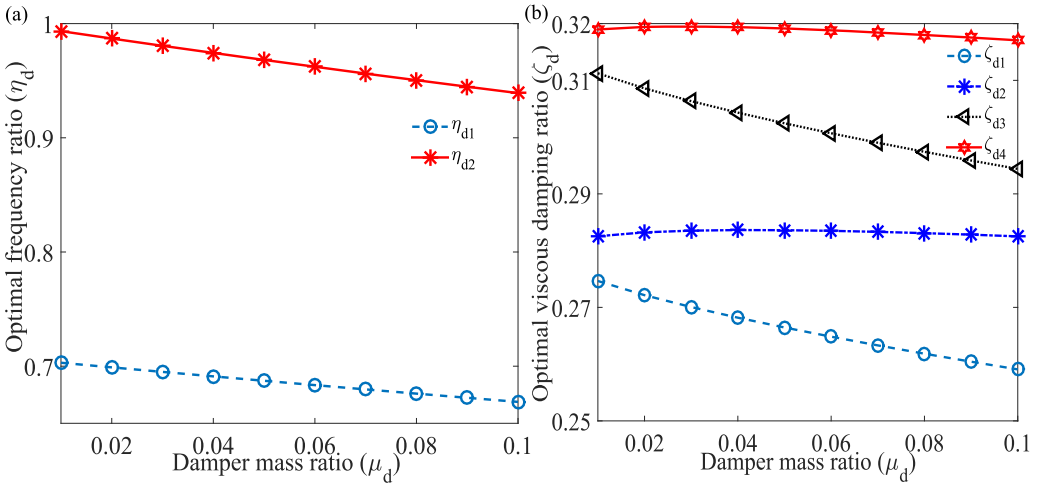

Figure 5. The variations of optimal (a) frequency and (b) viscous damping ratio of the structure controlled by AIVMD versus frequency ratio. Two solutions of Eq. (46) are applied for the optimal frequency ratio evaluation. Equations (50), (47), and (48) are applied for the evaluation of the optimal viscous damping ratio.

for optimal frequency ratio. Each solution has been accounted for and shows in Fig. 5(a). The optimal frequency ratio decreases for both solutions as the damper mass ratio increases. However, the first expression of Eq. (46) provides lower frequency ratios than the second expression of Eq. (46). Later, the optimal dynamic response graphs for each optimal frequency are drawn to investigate the efficiency of these solutions. These solutions are also utilized to achieve an optimal damping ratio for optimum AIVMD. Furthermore, the differences in the optimal damping ratio for optimum AIVMD are determined by varying the damper mass ratio and exhibited in Fig. 5(b). Equation (50) utilizes for this graph and appears that contains two solutions. $\alpha = 1.0$ considers drawing this figure. Therefore, two additional solutions for optimal damping ratio have been achieved for each optimal frequency ratio. Therefore, four solutions are achieved from Eq. (50) and shown in Fig. 5(b). The best possible outcomes are considered to design optimum AIVMD and utilized later for optimum dynamic response graphs. This parametric study, it observes that the optimal damping ratio decreases as the damper mass ratio increases. Thus, a higher damper mass ratio recommends for optimum AIVMD having a lower frequency and damping ratio at an affordable range. The optimal dynamic response diagrams are determined using these optimal system parameters to obtain their effectiveness. As a result, the variations of the optimal dynamic responses of the primary structures controlled by H_∞ optimized AIVMD versus frequency ratio for different values of viscous damping ratios of the dampers are shown in Fig. 6(a). The system parameters are utilized for this figure are $\mu_d = 0.04$, $\mu_b = 0.01$, and $\alpha = 1.0$. The first equations of Eqs. (46) and (50) are applied, which provide $\eta_{d1} = 0.6911$ and $\zeta_{d1} = 0.2682$ are determined. $\eta = 0.6792$ and $\eta = 1.018$ are the eigen frequencies at undamped condition, i.e., $\zeta_d = 0$. $\eta = 0.743$ and $\eta = 1.023$ are the resonating frequencies when $(\zeta_d)_{opt} = 0.2682$. Massive increments of dynamic responses have occurred at $\zeta_d = \infty$ with frequency points of $\eta = 0.8951$ and $\eta = 1.092$. The second equation of Eq. (46) has been utilized, and the optimal dynamic response diagram has been determined. Therefore, the variations of the optimal dynamic responses of the primary structures controlled by H_∞ optimized AIVMD versus frequency ratio for different values of viscous damping ratios of the dampers are shown in Fig. 6(b) with different solutions for optimal frequency and viscous damping ratios. The system parameters are utilized for this figure are $\mu_d = 0.04$, $\mu_b = 0.01$, and $\alpha = 1.0$. The second equations of Eqs. (46) and (50) are applied, which provide $\eta_{d2} = 0.9743$ and $\zeta_{d2} = 0.3043$ are determined. $\eta = 0.8937$ and $\eta = 1.09$ are the eigen frequencies at undamped condition, i.e., $\zeta_d = 0$. $\eta = 0.9568$ is the resonating frequency when $(\zeta_d)_{opt} = 0.3043$. Massive increments of dynamic responses have occurred at $\zeta_d = \infty$ with frequency points of $\eta = 0.9631$ and $\eta = 1.431$.

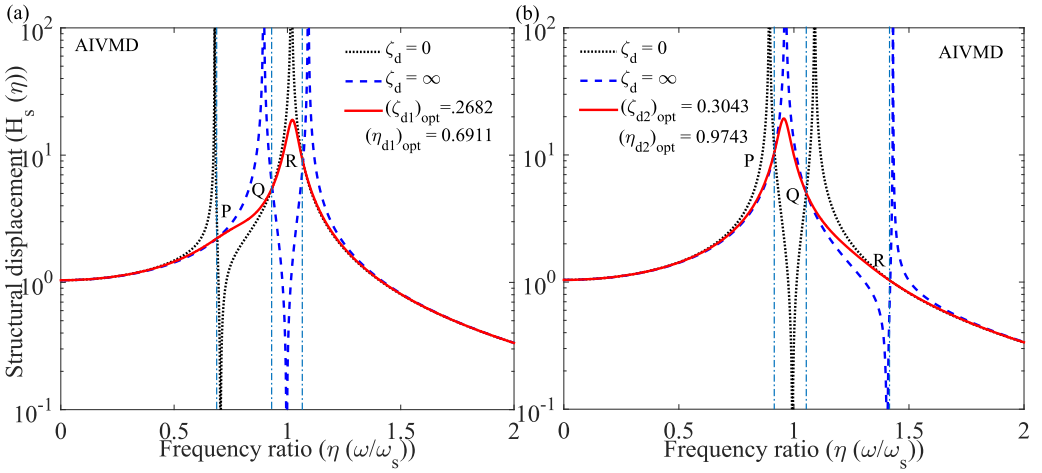

Figure 6. The variations of optimal dynamic responses of the main structure are controlled by AIVMD versus frequency ratio for different values of viscous damping ratio. Two different solutions for $\eta_{d1,d2}$ and $\zeta_{d1,d2}$ are applied for figure (a) and figure (b).

4.2. Additional viscoelastic mass damper inerters

The closed-form expressions for optimal design parameters of AVMDI have also been derived through the H_∞ optimization method when the controlled structures are subjected to harmonic excitations. To perform that the transfer function in Eq. (14) has been non-dimensionalized and expressed as

$$\begin{bmatrix} 2\ i\eta\ \zeta_s - \eta^2 + 1 & -2\ \dfrac{\eta_d{}^2(\mu_d+\mu_b)\left(\eta\ (\alpha+1)\zeta_d\ \mathrm{i} + 1/2\ \alpha\ \eta_d\right)}{2\ \mathrm{i}\eta\ \zeta_d + \alpha\ \eta_d} \\ -(\mu_d+\mu_b)\eta^2 & A_{22} \end{bmatrix} \begin{Bmatrix} X_s \\ X_d \end{Bmatrix} = -\begin{bmatrix} 1 \\ \mu_d \end{bmatrix} \frac{A_g}{\omega_s^2} \tag{54}$$

$$A_{22} = 2\ \frac{\left(-\mathrm{i}\eta^3\zeta_d - 1/2\ \alpha\ \eta^2\eta_d + \mathrm{i}\eta_d{}^2(\alpha+1)\zeta_d\ \eta + 1/2\ \alpha\ \eta_d{}^3\right)(\mu_d+\mu_b)}{2\ \mathrm{i}\eta\ \zeta_d + \alpha\ \eta_d}$$

The dynamic response of the primary structure has been derived as

$$H_s = \frac{X_s}{A_g}\omega_s^2 = \frac{\alpha\ \eta_d{}^3\mu_d - \alpha\ \eta^2\eta_d + \alpha\ \eta_d{}^3 + \mathrm{i}\left(2\ \eta\ \left((\mu_d+1)(\alpha+1)\eta_d{}^2 - \eta^2\right)\zeta_d\right)}{\Delta} \tag{55}$$

The dynamic response of AVMDI has been derived as

$$H_d = \frac{X_d}{A_g}\omega_s^2 = \frac{\eta^2\mu_b\alpha\ \eta_d - 4\ \eta^2\zeta_s\mu_d\zeta_d + \mu_d\alpha\ \eta_d + \mathrm{i}\left(2\ \eta\ \zeta_s\mu_d\alpha\ \eta_d + 2\ \eta^3\mu_b\zeta_d + 2\ \eta\ \zeta_d\ \mu_d\right)}{\Delta} \tag{56}$$

Δ has been derived as

$$\Delta = \begin{array}{c} \alpha\ \eta^2\eta_d{}^3\mu_b + \alpha\ \eta^2\eta_d{}^3\mu_d + 4\ \alpha\ \eta^2\eta_d{}^2\zeta_d\ \zeta_s - \eta^4\alpha\ \eta_d + \alpha\ \eta^2\eta_d{}^3 - 4\ \eta^4\zeta_d\ \zeta_s + 4\ \eta^2\eta_d{}^2\zeta_d\ \zeta_s \\ +\alpha\ \eta^2\eta_d - \alpha\ \eta_d{}^3 \\ +\mathrm{i}\begin{pmatrix} 2\ \alpha\ \eta^3\eta_d{}^2\zeta_d\ \mu_b + 2\ \alpha\ \eta^3\eta_d{}^2\zeta_d\ \mu_d + 2\ \alpha\ \eta^3\eta_d{}^2\zeta_d + 2\ \eta^3\eta_d{}^2\zeta_d\ \mu_b + 2\ \eta^3\eta_d{}^2\zeta_d\ \mu_d \\ +2\ \alpha\ \eta^3\eta_d\zeta_s - 2\ \alpha\ \eta\ \eta_d{}^3\zeta_s - 2\ \zeta_d\ \eta^5 + 2\ \eta^3\eta_d{}^2\zeta_d - 2\ \eta\ \alpha\ \eta_d{}^2\zeta_d + 2\ \eta^3\zeta_d - 2\ \eta\ \eta_d{}^2\zeta_d \end{pmatrix} \end{array} \tag{57}$$

The resultant of H_s has been summarized as

$$|H_s| = \sqrt{\frac{y_1^2 + \zeta_d^2 y_2^2}{y_3^2 + \zeta_d^2 y_4^2}} = \frac{y_2}{y_4}\sqrt{\frac{\frac{y_1^2}{y_2^2} + \zeta_d^2}{\frac{y_3^2}{y_4^2} + \zeta_d^2}} \tag{58}$$

From Eq. (55), the first restraint (Den Hartog 1985) for H_∞ optimization has been derived as

$$\left|\frac{y_1}{y_2}\right| = \left|\frac{y_3}{y_4}\right| \tag{59}$$

An equation has been derived after applying Eq. (59) and expressed as

$$\begin{aligned} &2\,\eta^6 - \left(\alpha\,{\eta_d}^2\mu_b + 2\,\alpha\,{\eta_d}^2\mu_d + 2\,\alpha\,{\eta_d}^2 + 2\,{\eta_d}^2\mu_b + 4\,{\eta_d}^2\mu_d + 4\,{\eta_d}^2 + 2\right)\eta^4 \\ &- \begin{pmatrix} -2\,\alpha\,{\eta_d}^4\mu_b\mu_d - 2\,\alpha\,{\eta_d}^4{\mu_d}^2 - 2\,\alpha\,{\eta_d}^4\mu_b - 4\,\alpha\,{\eta_d}^4\mu_d \\ -2\,{\eta_d}^4\mu_b\mu_d - 2\,{\eta_d}^4{\mu_d}^2 - 2\,\alpha\,{\eta_d}^4 - 2\,{\eta_d}^4\mu_b - 4\,{\eta_d}^4\mu_d \\ -\alpha\,{\eta_d}^2\mu_d - 2\,{\eta_d}^4 - 2\,\alpha\,{\eta_d}^2 - 2\,{\eta_d}^2\mu_d - 4\,{\eta_d}^2 \\ -2\,\alpha\,{\eta_d}^4\mu_d - 2\,\alpha\,{\eta_d}^4 - 2\,{\eta_d}^4\mu_d - 2\,{\eta_d}^4 \end{pmatrix}\eta^2 = 0 \end{aligned} \tag{60}$$

Equation (60) has been summarized as

$$\eta^6 + \left(-{\eta_1}^2 - {\eta_2}^2 - {\eta_3}^2\right)\eta^4 + \left({\eta_1}^2{\eta_2}^2 + {\eta_3}^2{\eta_1}^2 + {\eta_2}^2{\eta_3}^2\right)\eta^2 - {\eta_1}^2{\eta_2}^2{\eta_3}^2 = 0 \tag{61}$$

Therefore, the roots for Eq. (60) have been derived as

$$\begin{aligned} {\eta_1}^2 + {\eta_2}^2 + {\eta_3}^2 &= 1/2\,\alpha\,{\eta_d}^2\mu_b + \alpha\,{\eta_d}^2\mu_d + \alpha\,{\eta_d}^2 + {\eta_d}^2\mu_b + 2\,{\eta_d}^2\mu_d + 2\,{\eta_d}^2 + 1 \\ {\eta_1}^2{\eta_2}^2 + {\eta_3}^2{\eta_1}^2 + {\eta_2}^2{\eta_3}^2 &= \begin{matrix} \alpha\,{\eta_d}^4\mu_b\mu_d + \alpha\,{\eta_d}^4{\mu_d}^2 + \alpha\,{\eta_d}^4\mu_b + 2\,\alpha\,{\eta_d}^4\mu_d \\ +{\eta_d}^4\mu_b\mu_d + {\eta_d}^4{\mu_d}^2 + \alpha\,{\eta_d}^4 + {\eta_d}^4\mu_b \\ +2\,{\eta_d}^4\mu_d + 1/2\,\alpha\,{\eta_d}^2\mu_d + {\eta_d}^4 + \alpha\,{\eta_d}^2 \\ +{\eta_d}^2\mu_d + 2\,{\eta_d}^2 \end{matrix} \\ \eta_1^2\eta_2^2\eta_3^2 &= \alpha\,{\eta_d}^4\mu_d + \alpha\,{\eta_d}^4 + {\eta_d}^4\mu_d + {\eta_d}^4 \end{aligned} \tag{62}$$

From Eq. (55), the second constraint (Den Hartog 1985) has been derived as

$$(H_s)_{\eta_1,\eta_2} = \left|\frac{y_2}{y_4}\right| \tag{63}$$

$$\eta_1^2 + \eta_2^2 = 0 \tag{64}$$

Equation (64) substitutes in the first equation of Eq. (62). Hence, η_3^2 derives as

$${\eta_3}^2 = 1/2\,\alpha\,{\eta_d}^2\mu_b + \alpha\,{\eta_d}^2\mu_d + \alpha\,{\eta_d}^2 + {\eta_d}^2\mu_b + 2\,{\eta_d}^2\mu_d + 2\,{\eta_d}^2 + 1 \tag{65}$$

Equation (65) has been substitutes in the second and third equations of Eq. (62). Therefore, the closed-form expressions for ${\eta_{1,2}}^2$ have been derived as

$${\eta_{1,2}}^2 = \begin{matrix} \alpha\,{\eta_d}^4\mu_b\mu_d + \alpha\,{\eta_d}^4{\mu_d}^2 + \alpha\,{\eta_d}^4\mu_b + 2\,\alpha\,{\eta_d}^4\mu_d + {\eta_d}^4\mu_b\mu_d + {\eta_d}^4{\mu_d}^2 + 2\,{\eta_d}^2 \\ +\alpha\,{\eta_d}^4 + {\eta_d}^4\mu_b + 2\,{\eta_d}^4\mu_d + 1/2\,\alpha\,{\eta_d}^2\mu_d + {\eta_d}^4 + \alpha\,{\eta_d}^2 + {\eta_d}^2\mu_d \end{matrix} \tag{66}$$

$${\eta_{1,2}}^2 = \frac{2{\eta_d}^4(\mu_d + 1)(\alpha + 1)}{2 + (\mu_b + 2\;\mu_d + 2)(\alpha + 2){\eta_d}^2} \tag{67}$$

Equations (66) and (67) are equated, and the closed-form expression for optimal frequency ratio of AVMDI has been derived as

$$\begin{gathered}\left(2\ (\mu_d+1)(\mu_b+2\ \mu_d+2)(\mu_b+\mu_d+1)(\alpha+2)(\alpha+1)\right)\eta_d{}^4\\ +\begin{pmatrix}\alpha^2\mu_b\mu_d+2\ \alpha^2\mu_d{}^2+2\ \alpha^2\mu_b+6\ \alpha^2\mu_d+8\ \alpha\ \mu_b\mu_d\\ +12\ \alpha\ \mu_d{}^2+4\ \alpha^2+12\ \alpha\ \mu_b+28\ \alpha\ \mu_d\\ +8\ \mu_d\mu_b+12\ \mu_d{}^2+16\ \alpha+12\ \mu_b+28\ \mu_d+16\\ +2\ \alpha\ \mu_d+4\ \alpha+4\ \mu_d+8\end{pmatrix}\eta_d{}^2\ =0\end{gathered} \tag{68}$$

$$v_2\eta_d{}^4+v_1\eta_d{}^2+v_0=0 \tag{69}$$

$$(\eta_{d1})_{opt}^2=\frac{-v_1+\sqrt{v_1{}^2-4\ v_2v_0}}{2v_2}\quad\text{and}\quad(\eta_{d2})_{opt}^2=\frac{-v_1-\sqrt{v_1{}^2-4\ v_2v_0}}{2v_2} \tag{70}$$

After applying Eqs. (66) and (67), the closed-form expressions for $\eta_{1,2}^2$ are derived as

$$\eta_{1,2}^2=\pm\sqrt{\begin{gathered}\alpha\ \eta_d{}^4\mu_b\mu_d+\alpha\ \eta_d{}^4\mu_d{}^2+\alpha\ \eta_d{}^4\mu_b+2\ \alpha\ \eta_d{}^4\mu_d+\eta_d{}^4\mu_b\mu_d+\eta_d{}^4\mu_d{}^2+2\ \eta_d{}^2\\ +\alpha\ \eta_d{}^4+\eta_d{}^4\mu_b+2\ \eta_d{}^4\mu_d+1/2\ \alpha\ \eta_d{}^2\mu_d+\eta_d{}^4+\alpha\ \eta_d{}^2+\eta_d{}^2\mu_d\end{gathered}} \tag{71}$$

$$\eta_{1,2}^2=\pm\sqrt{\frac{2\eta_d{}^4(\mu_d+1)(\alpha+1)}{2+(\mu_b+2\ \mu_d+2)(\alpha+2)\eta_d{}^2}} \tag{72}$$

The mathematical expressions for determining the closed-form expression for the optimal viscous damping ratio of AVMDI have been derived as

$$\left.\frac{\partial|H_s(\eta)|^2}{\partial\eta^2}\right|_{\eta_{1,2}^2}=0\quad\text{and}\quad(\zeta_d)_{opt}=\sqrt{\frac{\zeta_{d1}^2+\zeta_{d2}^2}{2}} \tag{73}$$

Therefore, the closed-form expression for the optimal viscous damping ratio of AVMDI has been derived as

$$p_2\zeta_d^4+p_1\zeta_d^2+p_0=0\quad\text{and}\quad\zeta_{d1,d2}^2=\frac{-p_1\pm\sqrt{-4\ p_2p_0+p_1{}^2}}{2p_2} \tag{74}$$

The closed-form expressions for p_2, p_1, and p_0 have been derived as

$$p_2=-32\begin{pmatrix}(\alpha+1)^2(\mu_d+1)(\mu_b+\mu_d+1)\eta_d{}^4\\ -2\ (\alpha+1)\left((\mu_d+1)u-1/2\ \mu_d\right)\eta_d{}^2+u^2\end{pmatrix}u^2\left(-(\mu_d+1)(\alpha+1)\eta_d{}^2+u\right)\\ \left(-(-1+(\mu_b+\mu_d+1)u)(\alpha+1)\eta_d{}^2+u^2-u\right) \tag{75}$$

$$p_0=\frac{\left(-2\ \left((1+(-\mu_b-\mu_d-1)u)\eta_d{}^2+u^2-u\right)\eta_d{}^4\right)}{\left((\mu_d+1)(\mu_d+\mu_b+1)\eta_d{}^4+((-2\ \mu_d-2)u+\mu_d)\eta_d{}^2+u^2\right)\left((-\mu_d-1)\eta_d{}^2+u\right)\alpha^4} \tag{76}$$

where $u=\eta_{1,2}^2$. The variations of the optimal frequency ratio of the AVMDI versus damper mass ratio are shown in Fig. 7(a). $\alpha=1.0$ is accounted for in this graph. Equation (70) contains two exact closed-form expressions for optimal frequency ratio. Each solution has been accounted for and shows in Fig. 7(a). The optimal frequency ratio decreases for both solutions as the damper

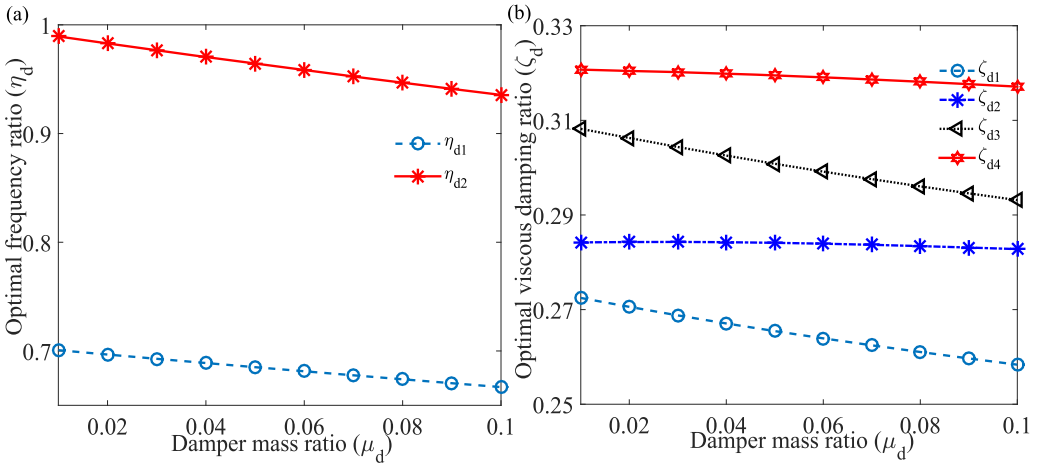

Figure 7. The variations of optimal (a) frequency and (b) viscous damping ratio of the structure controlled by AVMDI versus frequency ratio. Two solutions of Eq. (70) are applied for frequency ratio evaluation. Equations (74), (71), and (72) are applied for evaluation of viscous damping ratio.

mass ratio increases. However, the first expression of Eq. (70) provides lower frequency ratios than the second expression of Eq. (70). Later, the optimal dynamic response graphs for each optimal frequency are drawn to investigate the efficiency of these solutions. These solutions are also utilized to achieve an optimal damping ratio for optimum AVMDI. Furthermore, the differences in the optimal damping ratio for optimum AVMDI are determined by varying the damper mass ratio and exhibited in Fig. 7(b). Equation (74) utilizes for this graph and appears that contains two solutions. $\alpha = 1.0$ considers drawing this figure. Therefore, two additional solutions for optimal damping ratio have been achieved for each optimal frequency ratio. Therefore, four solutions are achieved from Eq. (74) and shown in Fig. 7(b). The best possible outcomes are considered to design optimum AVMDI and utilized later for optimum dynamic response graphs. This parametric study observes that the optimal damping ratio decreases as the damper mass ratio increases. Thus, a higher damper mass ratio recommends for optimum AVMDI, having a lower frequency and damping ratio at an affordable range. The optimal dynamic response diagrams are determined using these optimal system parameters to obtain their effectiveness. As a result, the variations of the optimal dynamic responses of the primary structures controlled by H_∞ optimized AVMDI versus frequency ratio for different values of viscous damping ratios of the dampers are shown in Fig. 8(a). The system parameters are utilized for this figure are $\mu_d = 0.04$, $\mu_b = 0.01$, and $\alpha = 1.0$. The first equations of Eqs. (70) and (74) are applied, which provide $\eta_{d2} = 0.6889$ and $\zeta_{d2} = 0.2671$ are determined. $\eta = 0.6744$ and $\eta = 1.022$ are the eigen frequencies at undamped condition, i.e., $\zeta_d = 0$. $\eta = 0.7079$ and $\eta = 1.028$ are the resonating frequencies when $(\zeta_d)_{opt} = 0.2671$. Massive increments of dynamic responses have occurred at $\zeta_d = \infty$ with frequency points of $\eta = 0.8834$ and $\eta = 1.103$. The second equation of Eq. (70) has been utilized, and the optimal dynamic response diagram has been determined. Therefore, the variations of the optimal dynamic responses of the primary structures controlled by H_∞ optimized AVMDI versus frequency ratio for different values of viscous damping ratios of the dampers are shown in Fig. 8(b) with different solutions for optimal frequency and viscous damping ratios. The system parameters are utilized for this figure are $\mu_d = 0.04$, $\mu_b = 0.01$, and $\alpha = 1.0$. The second equations of Eqs. (70) and (74) are applied, which provide $\eta_{d2} = 0.9704$ and $\zeta_{d2} = 0.2842$ are determined. $\eta = 0.8817$ and $\eta = 1.101$ are the eigen frequencies at undamped condition, i.e., $\zeta_d = 0$. $\eta = 0.9442$ is the resonating frequency when $(\zeta_d)_{opt} = 0.2842$. Massive increments of dynamic responses have occurred at $\zeta_d = \infty$ with frequency points of $\eta = 0.9548$ and $\eta = 1.437$. The optimal dynamic responses are also evaluated with structural damping, and according to those values,

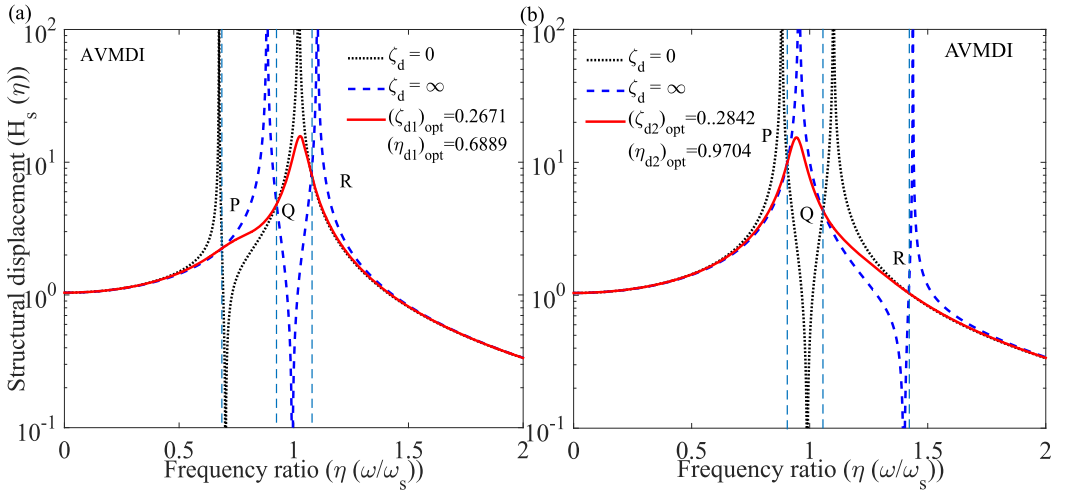

Figure 8. The variations of optimal dynamic responses of the main structure are controlled by AVMDI versus frequency ratio for different values of viscous damping ratio. Two different solutions for $\eta_{d1,d2}$ and $\zeta_{d1,d2}$ are applied for figure (a) and figure (b).

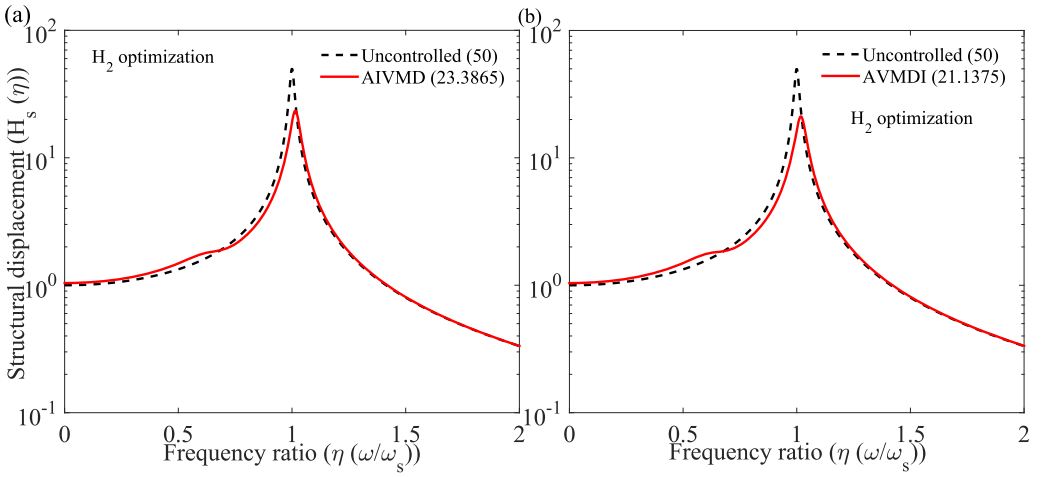

Figure 9. The variations of optimal dynamic responses of the SDOF systems equipped with H_2 optimized (a) AIVMD and (b) AVMDI. $\zeta_s = 0.01$.

each optimum novel damper's dynamic response capacity is determined. Therefore, to perform that, the variations of the optimal dynamic responses of the SDOF system equipped with H_2 optimized AIVMD are determined and shown in Fig. 9(a). $\zeta_s = 0.01$ considers. The maximum dynamic responses of the uncontrolled structures are obtained as 50. H_2 optimized AIVMD controlled structure's maximum dynamic response obtains as 23.3865. Thus, 53.23% dynamic response reduction capacity of H_2 optimized AIVMD. The variations of the optimal dynamic responses of the SDOF system equipped with H_2 optimized AVMDI are determined and shown in Fig. 9(b). $\zeta_s = 0.01$ considers. The maximum dynamic responses of the uncontrolled structures are obtained as 50. H_2 optimized AVMDI controlled structure's maximum dynamic response obtains as 21.1375. Thus, 57.73% dynamic response reduction capacity of H_2 optimized AVMDI. The variations of the optimal dynamic responses of the SDOF system equipped with H_∞ optimized AIVMD are determined and shown in Fig. 10(a). $\zeta_s = 0.01$ considers. The maximum dynamic responses of the uncontrolled structures are obtained as 50. H_∞ optimized AIVMD controlled structure's maximum dynamic response obtains as 13.5147. Thus, 72.97% dynamic

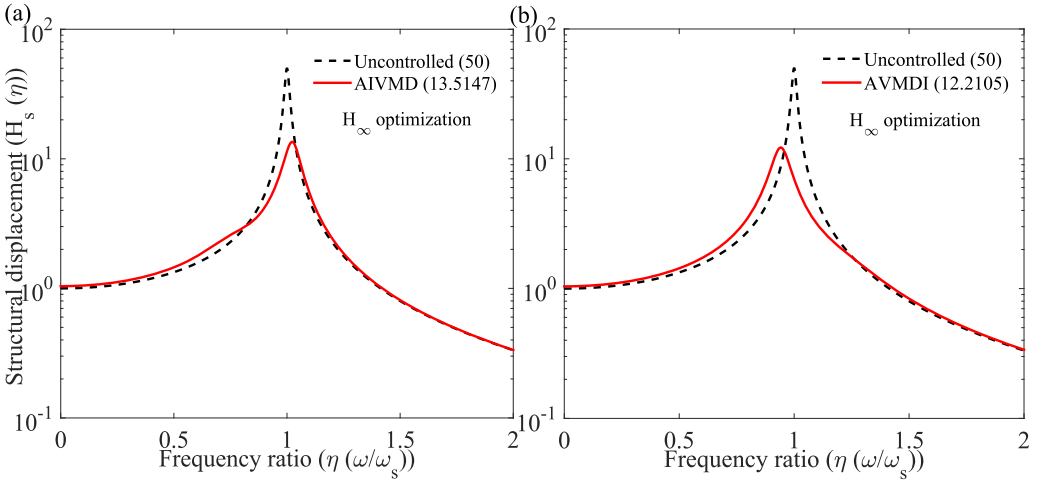

Figure 10. The variations of optimal dynamic responses of the SDOF systems equipped with H_∞ optimized (a) AIVMD and (b) AVMDI. $\zeta_s = 0.01$.

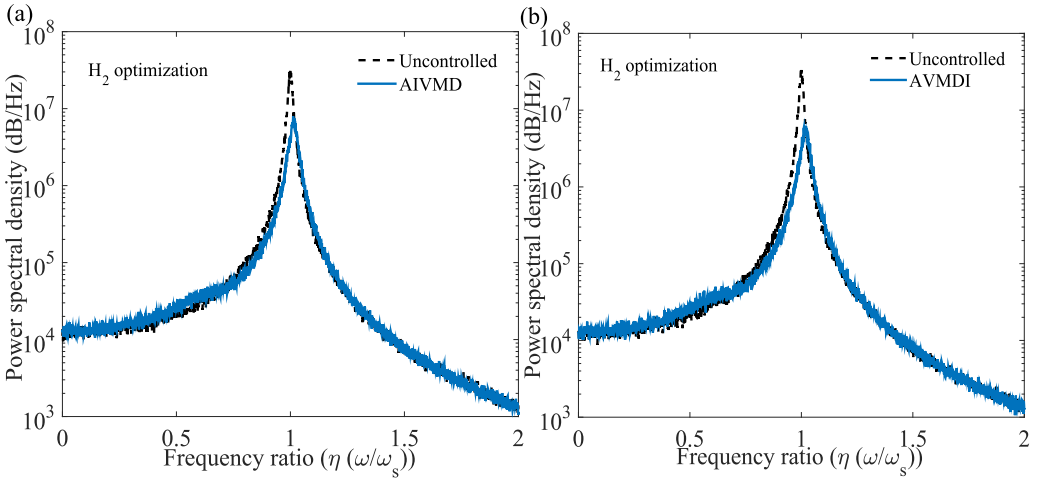

Figure 11. The variations of optimal dynamic responses of the SDOF systems equipped with H_2 optimized (a) AIVMD and (b) AVMDI subjected to rand-white noise. $\zeta_s = 0.01$.

response reduction capacity of H_∞ optimized AIVMD. The variations of the optimal dynamic responses of the SDOF system equipped with H_∞ optimized AVMDI are determined and shown in Fig. 10(b). $\zeta_s = 0.01$ considers. The maximum dynamic responses of the uncontrolled structures are obtained as 50. H_∞ optimized AVMDI controlled structure's maximum dynamic response obtains as 12.2105. Thus, 75.57% dynamic response reduction capacity of H_∞ optimized AVMDI. The variations of the optimal dynamic responses of the SDOF system equipped with H_2 optimized AIVMD subjected to random-white noise are determined and shown in Fig. 11(a). $\zeta_s = 0.01$ considers. The maximum dynamic responses of the uncontrolled structures are obtained as 3.09×10^7 dB/Hz. H_2 optimized AIVMD controlled structure's maximum dynamic response obtains as 7.95×10^6 dB/Hz. Thus, 74.24% dynamic response reduction capacity of H_2 optimized AIVMD. The variations of the optimal dynamic responses of the SDOF system equipped with H_2 optimized AVMDI subjected to random-white noise are determined and shown in Fig. 11(b). $\zeta_s = 0.01$ considers. The maximum dynamic responses of the uncontrolled structures are obtained as 3.49×10^7 dB/Hz. H_2 optimized AIVMD controlled structure's maximum dynamic response

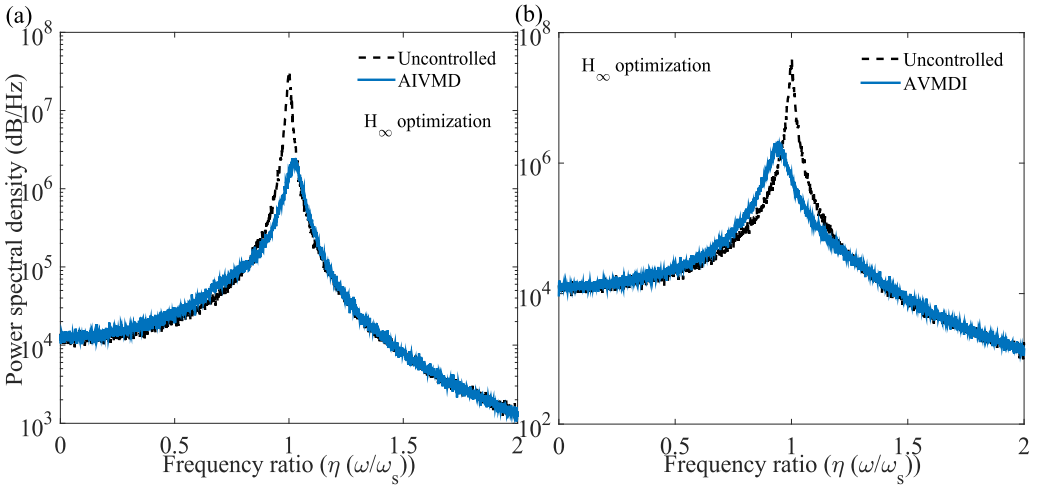

Figure 12. The variations of optimal dynamic responses of the SDOF systems equipped with H_∞ optimized (a) AIVMD and (b) AVMDI subjected to rand-white noise. $\zeta_s = 0.01$.

obtains as 6.23×10^6 dB/Hz. Thus, 82.17% dynamic response reduction capacity of H_2 optimized AVMDI. The variations of the optimal dynamic responses of the SDOF system equipped with H_∞ optimized AIVMD subjected to random-white noise are determined and shown in Fig. 12(a). $\zeta_s = 0.01$ considers. The maximum dynamic responses of the uncontrolled structures are obtained as 3.15×10^7 dB/Hz. H_2 optimized AIVMD controlled structure's maximum dynamic response obtains as 2.48×10^6 dB/Hz. Thus, 92.14% dynamic response reduction capacity of H_∞ optimized AIVMD. The variations of the optimal dynamic responses of the SDOF system equipped with H_∞ optimized AVMDI subjected to random-white noise are determined and shown in Fig. 12(b). $\zeta_s = 0.01$ considers. The maximum dynamic responses of the uncontrolled structures are obtained as 3.83×10^7 dB/Hz. H_2 optimized AVMDI controlled structure's maximum dynamic response obtains as 2.16×10^6 dB/Hz. Thus, 94.36% dynamic response reduction capacity of H_∞ optimized AIVMD.

5. Summary and conclusions

The additional inerter-based viscoelastic mass dampers (AIVMD) and additional viscoelastic mass damper inerters (AVMDI) are introduced in this article. These novel dampers are applied to the single degree of freedom systems to reduce their dynamic responses subjected to base excitations. The harmonic and random-white noise excitations are applied to the controlled structures as base excitations. In addition, the optimal closed-form solutions in terms of exact closed-form expressions for design parameters are derived using H_2 and H_∞ optimization process. Hence, using these optimal closed-form solutions, the optimum performance of AIVMD and AVMDI has been achieved. In addition, the dynamic reduction capacities of optimum AIVMD and AVMDI are determined mathematically. Overall, the newly derived exact mathematical formulations for the optimal design parameters, such as natural frequency and damping ratios of the novel dampers, namely additional inerter-based viscoelastic mass dampers (AIVMD) and additional viscoelastic mass damper inerters (AVMDI) are the significant novelty of the article. According to the parametric study, a higher damper mass ratio, a higher inerter mass ratio, and a higher stiffness ratio are recommended to achieve optimum dynamic response reduction capacity from H_2 and H_∞ optimized AIVMD and AVMDI with a lower frequency and damping ratios at affordable ranges. The dynamic response reduction capacity of each optimum AIVMD and AVMDI has been determined for harmonic and random-white noise excitations. Therefore, according to harmonic

excitation-induced dynamic analysis, the dynamic response reduction capacities of H_2 optimized AIVMD and AVMDI are determined as 53.23% and 57.73% and H_∞ optimized AIVMD and AVMDI's dynamic response reduction capacities are obtained as 72.97% and 75.57%. In addition, the random-white excitations are also applied to estimate each damper's dynamic response reduction capacity to verify the accuracy of each optimal closed-form solution for optimal design parameters. Therefore, for H_2 optimized AIVMD and AVMDI, the dynamic response reduction capacity of H_2 optimized AIVMD and AVMDI are determined as 74.24% and 82.17% and H_∞ optimized AIVMD and AVMDI's dynamic response reduction capacities are obtained as 92.14% and 94.36%. Therefore, the newly derived optimal closed-form solutions are mathematically accurate and relevant for practical applications. The applications of the additional inerter-based viscoelastic mass dampers and additional viscoelastic mass damper inerters to the multi degree of freedom systems (MDOF) system, such as for dynamic response mitigation of tall buildings with derivations of exact closed-form solutions for optimal system parameters are the future scopes of this study.

Acknowledgement

The authors would like to acknowledge the Inspire faculty grant, grant number DST/INSPIRE/04/2018/000052 for partial financial support for the project. SC would like to acknowledge the MHRD grant received from IIT Delhi during the period of this research work.

Disclosure statement

The authors declare that they have no known competing financial interests or personal relationships that could have appeared to influence the work reported in this article.

ORCID

Sudip Chowdhury http://orcid.org/0000-0001-6218-4843
Arnab Banerjee http://orcid.org/0000-0002-3157-6200
Sondipon Adhikari http://orcid.org/0000-0003-4181-3457

Data availability statement

All data, models, and code generated or used during the study appear in the submitted article.

References

Adhikari, S., and B. Pascual. 2009. Eigenvalues of linear viscoelastic systems. *Journal of Sound and Vibration* 325 (4-5):1000–11. doi:10.1016/j.jsv.2009.04.008.

Adhikari, S., and J. Woodhouse. 2001a. Identification of damping: Part 1, viscous damping. *Journal of Sound and Vibration* 243 (1):43–61. doi:10.1006/jsvi.2000.3391.

Adhikari, S., and J. Woodhouse. 2001b. Identification of damping: Part 2, non-viscous damping. *Journal of Sound and Vibration* 243 (1):63–88. doi:10.1006/jsvi.2000.3392.

Batou, A., and S. Adhikari. 2019. Optimal parameters of viscoelastic tuned-mass dampers. *Journal of Sound and Vibration* 445:17–28. doi:10.1016/j.jsv.2019.01.010.

Chen, M. Z., and Y. Hu. 2019. *Inerter and its application in vibration control systems*. Springer.

Chowdhury, S., and A. Banerjee. 2022a. The exact closed-form equations for optimal design parameters of enhanced inerter-based isolation systems. *Journal of Vibration and Control* :10775463221133428. doi:10.1177/10775463221133428.

Chowdhury, S., and A. Banerjee. 2022b. The exact closed-form expressions for optimal design parameters of resonating base isolators. *International Journal of Mechanical Sciences* 224:107284. doi:10.1016/j.ijmecsci.2022.107284.

Chowdhury, S., A. Banerjee, and S. Adhikari. 2021. Enhanced seismic base isolation using inertial amplifiers. In *Structures*, vol. 33, 1340–53. Elsevier. doi:10.1016/j.istruc.2021.04.089.
Chowdhury, S., A. Banerjee, and S. Adhikari. 2022a. The optimal design of dynamic systems with negative stiffness inertial amplifier tuned mass dampers. *Applied Mathematical Modelling* 114:694–721. doi:10.1016/j.apm.2022.10.011.
Chowdhury, S., A. Banerjee, and S. Adhikari. 2022b. Optimal negative stiffness inertial-amplifier-base-isolators: Exact closed-form expressions. *International Journal of Mechanical Sciences* 218:107044. doi:10.1016/j.ijmecsci.2021.107044.
Chowdhury, S., A. Banerjee, and S. Adhikari. 2023. Optimal design of inertial amplifier base isolators for dynamic response control of multi-storey buildings. *International Journal of Structural Stability and Dynamics* 23 (05): 2350047. doi:10.1142/S0219455423500475.
Chowdhury, S., A. Banerjee, and S. Adhikari. 2023. The optimum inertial amplifier tuned mass dampers for nonlinear dynamic systems. *International Journal of Applied Mechanics* 15 (02):2350009. doi:10.1142/S1758825123500096.
De Domenico, D., and G. Ricciardi. 2018. Earthquake-resilient design of base isolated buildings with tmd at basement: Application to a case study. *Soil Dynamics and Earthquake Engineering* 113:503–21. doi:10.1016/j.soildyn.2018.06.022.
Deastra, P., D. Wagg, N. Sims, and M. Akbar. 2020. Tuned inerter dampers with linear hysteretic damping. *Earthquake Engineering & Structural Dynamics* 49 (12):1216–35. doi:10.1002/eqe.3287.
Den Hartog, J. P. 1985. *Mechanical vibrations*. Courier Corporation.
Djerouni, S., M. Abdeddaim, S. Elias, and R. Rupakhety. 2021. Optimum double mass tuned damper inerter for control of structure subjected to ground motions. *Journal of Building Engineering* 44:103259. doi:10.1016/j.jobe.2021.103259.
Elias, S., and V. Matsagar. 2018. Wind response control of tall buildings with a tuned mass damper. *Journal of Building Engineering* 15:51–60. doi:10.1016/j.jobe.2017.11.005.
Frahm, H. 1909. *Devices for damping vibration of bodies*. US Patent.
Giaralis, A., and F. Petrini. 2017. Wind-induced vibration mitigation in tall buildings using the tuned mass-damper-inerter (tmdi). *Journal of Structural Engineering* 143 (9):04017127. doi:10.1061/(ASCE)ST.1943-541X.0001863.
Jahangiri, V., C. Sun, and F. Kong. 2021. Study on a 3d pounding pendulum tmd for mitigating bi-directional vibration of offshore wind turbines. *Engineering Structures* 241:112383. doi:10.1016/j.engstruct.2021.112383.
Kaveh, A., M. Fahimi Farzam, H. Hojat Jalali, and R. Maroofiazar. 2020. Robust optimum design of a tuned mass damper inerter. *Acta Mechanica* 231 (9):3871–96. doi:10.1007/s00707-020-02720-9.
Kaynia, A. M., D. Veneziano, and J. M. Biggs. 1981. Seismic effectiveness of tuned mass dampers. *Journal of the Structural Division* 107 (8):1465–84. doi:10.1061/JSDEAG.0005760.
Kuhnert, W. M., P. J. P. Gonçalves, D. F. Ledezma-Ramirez, and M. J. Brennan. 2021. Inerter-like devices used for vibration isolation: A historical perspective. *Journal of the Franklin Institute* 358 (1):1070–86. doi:10.1016/j.jfranklin.2020.11.007.
Leung, A. Y., H. Zhang, C. Cheng, and Y. Lee. 2008. Particle swarm optimization of tmd by non-stationary base excitation during earthquake. *Earthquake Engineering & Structural Dynamics* 37 (9):1223–46. doi:10.1002/eqe.811.
Liu, C., L. Chen, H. P. Lee, Y. Yang, and X. Zhang. 2022. A review of the inerter and inerter-based vibration isolation: Theory, devices, and applications. *Journal of the Franklin Institute* 359 (14):7677–707. doi:10.1016/j.jfranklin.2022.07.030.
Ma, R., K. Bi, and H. Hao. 2021. Inerter-based structural vibration control: A state-of-the-art review. *Engineering Structures* 243:112655. doi:10.1016/j.engstruct.2021.112655.
Marano, G. C., R. Greco, and S. Sgobba. 2010. A comparison between different robust optimum design approaches: Application to tuned mass dampers. *Probabilistic Engineering Mechanics* 25 (1):108–18. doi:10.1016/j.probengmech.2009.08.004.
Marian, L., and A. Giaralis. 2014. Optimal design of a novel tuned mass-damper–inerter (tmdi) passive vibration control configuration for stochastically support-excited structural systems. *Probabilistic Engineering Mechanics* 38:156–64. doi:10.1016/j.probengmech.2014.03.007.
Morga, M., and G. C. Marano. 2014. Optimization criteria of tmd to reduce vibrations generated by the wind in a slender structure. *Journal of Vibration and Control* 20 (16):2404–16. doi:10.1177/1077546313478296.
Papageorgiou, C., N. E. Houghton, and M. C. Smith. 2009. Experimental testing and analysis of inerter devices. *Journal of Dynamic Systems, Measurement, and Control* 131 (1) doi:10.1115/1.3023120.
Pellizzari, F., G. Marano, A. Palmeri, R. Greco, and M. Domaneschi. 2022. Robust optimization of mtmd systems for the control of vibrations. *Probabilistic Engineering Mechanics* 70:103347. doi:10.1016/j.probengmech.2022.103347.
Petrini, F., A. Giaralis, and Z. Wang. 2020. Optimal tuned mass-damper-inerter (tmdi) design in wind-excited tall buildings for occupants' comfort serviceability performance and energy harvesting. *Engineering Structures* 204: 109904. doi:10.1016/j.engstruct.2019.109904.
Qiao, H., P. Huang, D. De Domenico, and Q. Wang. 2022. Structural control of high-rise buildings subjected to multi-hazard excitations using inerter-based vibration absorbers. *Engineering Structures* 266:114666. doi:10.1016/j.engstruct.2022.114666.

Rathi, A. K., and A. Chakraborty. 2017. Reliability-based performance optimization of tmd for vibration control of structures with uncertainty in parameters and excitation. *Structural Control and Health Monitoring* 24 (1):e1857. doi:10.1002/stc.1857.

Roberts, J. B., and P. D. Spanos. 2003. *Random vibration and statistical linearization.* Courier Corporation.

Ruiz, R., A. Taflanidis, A. Giaralis, and D. Lopez-Garcia. 2018. Risk-informed optimization of the tuned mass-damper-inerter (tmdi) for the seismic protection of multi-storey building structures. *Engineering Structures* 177: 836–50. doi:10.1016/j.engstruct.2018.08.074.

Shen, W., A. Niyitangamahoro, Z. Feng, and H. Zhu. 2019. Tuned inerter dampers for civil structures subjected to earthquake ground motions: Optimum design and seismic performance. *Engineering Structures* 198:109470. doi: 10.1016/j.engstruct.2019.109470.

Smith, M. C. 2002. Synthesis of mechanical networks: The inerter. *IEEE Transactions on Automatic Control* 47 (10):1648–62. doi:10.1109/TAC.2002.803532.

Wagg, D. J. 2021. A review of the mechanical inerter: Historical context, physical realisations and nonlinear applications. *Nonlinear Dynamics* 104 (1):13–34. doi:10.1007/s11071-021-06303-8.

Wang, Q., H. Qiao, D. De Domenico, Z. Zhu, and Z. Xie. 2019. Wind-induced response control of high-rise buildings using inerter-based vibration absorbers. *Applied Sciences* 9 (23):5045. doi:10.3390/app9235045.

Zhang, Z., and B. Fitzgerald. 2020. Tuned mass-damper-inerter (tmdi) for suppressing edgewise vibrations of wind turbine blades. *Engineering Structures* 221:110928. doi:10.1016/j.engstruct.2020.110928.

Zhang, Z., and C. Høeg. 2021. Inerter-enhanced tuned mass damper for vibration damping of floating offshore wind turbines. *Ocean Engineering* 223:108663. doi:10.1016/j.oceaneng.2021.108663.

Zhao, Z., Q. Chen, R. Zhang, C. Pan, and Y. Jiang. 2020. Energy dissipation mechanism of inerter systems. *International Journal of Mechanical Sciences* 184:105845. doi:10.1016/j.ijmecsci.2020.105845.

Zhao, Z., R. Zhang, Y. Jiang, and C. Pan. 2019. A tuned liquid inerter system for vibration control. *International Journal of Mechanical Sciences* 164:105171. doi:10.1016/j.ijmecsci.2019.105171.

Zheng, Y.-L., L.-Y. Li, and T.-J. Zhang. 2022. Energy analysis and optimization of inerter-based systems. *Journal of Vibration and Control* 28 (9-10):985–97. doi:10.1177/1077546320987730.

Zuo, H., K. Bi, and H. Hao. 2017. Using multiple tuned mass dampers to control offshore wind turbine vibrations under multiple hazards. *Engineering Structures* 141:303–15. doi:10.1016/j.engstruct.2017.03.006.